Addressing the Grid size Sensitivity Issue in Large eddy Simulations of Stable Boundary Layers

Yi Dai

Master Thesis in July 14 2020
TU Delft - Environmental Engineering

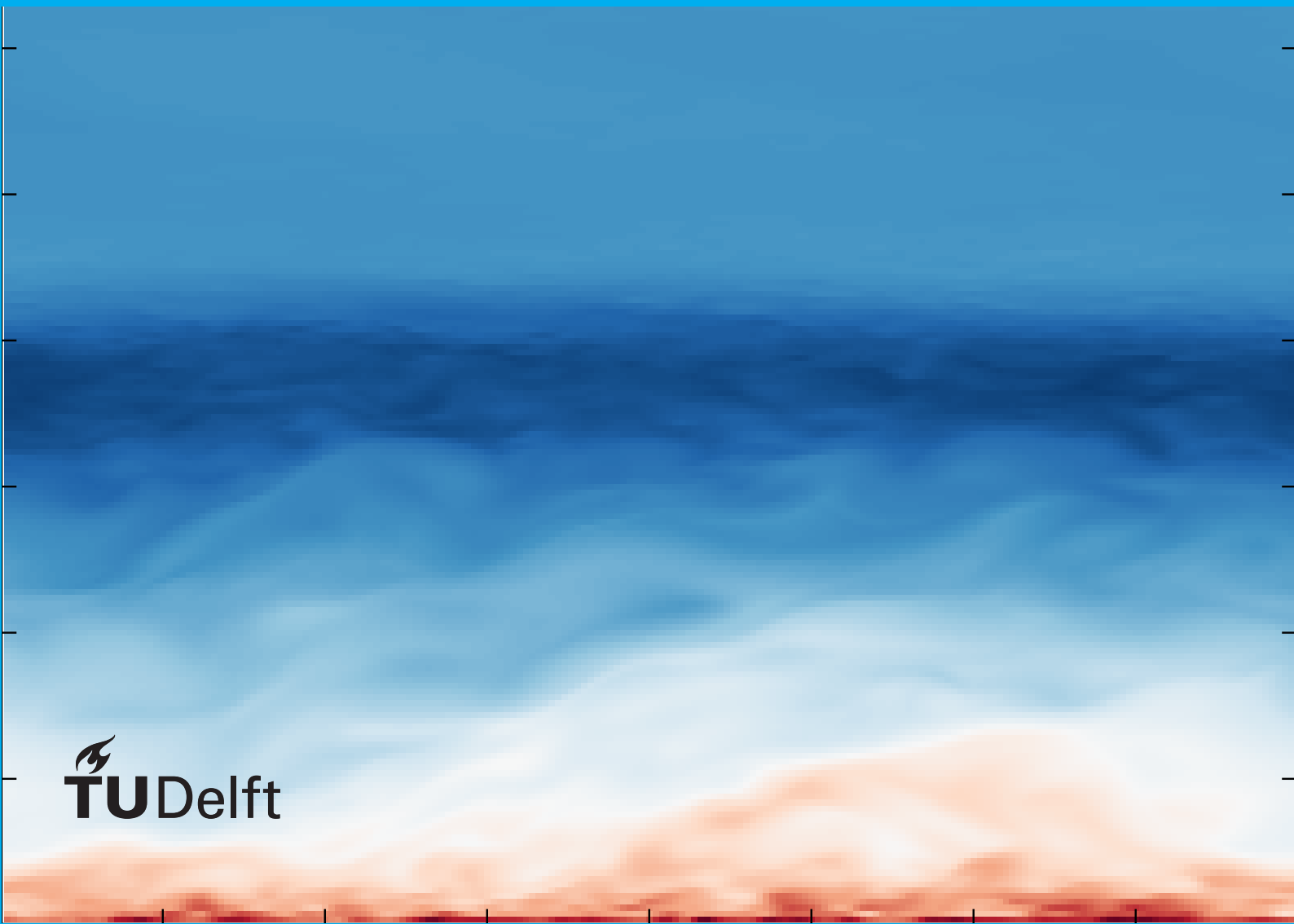

TU Delft

Cover figure: the vertical slice of streamwise velocity at 200m distance in normal direction under stably stratified condition (GABLS1 case, the scale shown in the figure have constant interval of 50m)

Addressing the Grid size Sensitivity Issue in Large eddy Simulations of Stable Boundary Layers

by

Yi Dai

to obtain the degree of Master of Science
at the Delft University of Technology,
to be defended publicly on July 14, 2020 at 09:00 AM.

Student number:	4817362	
supervisor:	Dr. Sukanta Basu,	TU Delft
Thesis committee:	Dr. Stephan de Roode,	TU Delft
	Dr. Clara Garcia-Sanchez,	TU Delft

This thesis is confidential and cannot be made public until July 14, 2020.

An electronic version of this thesis is available at `http://repository.tudelft.nl/`.

TU Delft

Abstract

In current study, several fundamental and inherent problems in original Deardorff subgrid model are identified under stably stratified condition. It is found that the mixing length parameterization in this subgrid model is at the root of a long trouble problem of grid size sensitivity in large-eddy simulation (LES). A new formulation of mixing length is proposed under the consideration of some basic elements including the presence of surface, the dependence of grid size Δ and a smoothing interpolation. The performance of this modified scheme is remarkable regarding the improvement of the simulation quality and accuracy. In other words, not only is the convergence of the simulated results from a range of grid size achieved but also in the precise intensity of physical variables are modelled. The only discrepancies display in the variance of temperature in the middle of boundary layer and high turbulent kinetic energy near the surface.

To further experiment the performance of the new scheme under different scenarios, the cases of different stability condition, an independent LES code with same modification, the cases of different advection schemes and different prescribed parameters are explored. In very stable condition, the first order variables from the modified scheme are in reasonable range but with some spreads compared to the results from a dynamic code. The deviation of second order statistics shows that the proposed formulation of mixing length meets limitations due to the complex interaction between the surface and turbulent flow in shallower boundary layer. The modified scheme is model system independent based on the similar improvement of simulation results in an independent LES code system. The sensitivity of advection schemes is surprisingly hardly found in new proposed SGS model. The cases of tested parameters further verifies the limitation of original Deardroff subgrid model.

Acknowledgement

I would like to specially thank Sukanta for his patient guidance, valuable suggestions, generous availability through out the course of this research. This work would not have been possible without his keen insight and overflowing enthusiasm on LES. An interesting question brought up by Sukanta during the introduction of first lecture of atmospheric science walked me in this field (*What is your career goal*). Then it leads to this research. I would also like to thank my committee, Stephan for the technical support on DALES and valuable time for evaluating this work; Clara for the time and energy put in the assessment.

Thanks to Vrlab and Sukanta's machine for the powerful computational support. The expensive simulations are not possible on my own laptop and it cost much to run them on cloud virtual machine. I also want to thank Erwin de Beus for technical support and fast response on the question in terms of Vrlab.

Finally I would like to thank my family for unlimited support on my master journey and friends for the warm encouragement during the two years. The accompanying time in Studoc starting 8 clock in the morning and the fundamental interpretations of my research when I try to explain with my friends are much appreciated. This research would not be here without their valuable support. I also want to give my thanks to Tchaikovsky for his elegant pieces accompanying me days and nights during the drafting of this master thesis.

Contents

1 Introduction

In the field of large-eddy simulation (LES), the discretization of the domain is crucial and influential to the simulated results. A code system with an isotropic and static mesh is usually implemented in the numerical modelling of atmospheric boundary layer (ABL). Without the priori knowledge of the cases, the grid size is hard to define regarding the representation of physical variables on the grid, the effect of subgrid-scale (SGS) model and the complexity of turbulent interaction under various topography and meteorological condition. The discrepancy of simulated value on a grid generally happens in the area or time where the sharp gradient exists (e.g., inversion layer; heterogeneous surface). In terms of the effect of subgrid-scale model, the dependence is related to the filter width which is set as the grid size or relates to grid size in implicit or explicit filter function respectively. Furthermore, the requirement that more than 80% of turbulent kinetic energy (TKE) is resolved in LES (Pope 2004) should be taken into consideration.

The sensitivity issue of grid size in large-eddy simulation under stable boundary layer (SBL) have been reported in many studies. In the study of Beare et al. (2006), the first intercomparison study of large-eddy simulation involved eleven participants and displayed the sensitivity of grid size based on the case of Global Energy and Water Exchanges (GEWEX) Atmospheric Boundary Layer Study (GABLS) (Holtslag 2006). From then on, similar features of sensitivity are shown in turbulent statistics from many other studies based on GABLS1 case (Matheou (2016), Sullivan et al. (2016), Maronga et al. (2020)). Especially, the simulation results from Sullivan et al. (2016) still displayed the grid sensitivity with the implementation of fine resolution down to 2m, 0.78m and 0.39m. Maronga et al. (2020) attempted to solve this issue by improvement of surface boundary layer condition. An elevated height is used to calculate the surface flux based on flux-profile relationship. However, this approach is only practical for the improvement of surface flux instead of vertical profiles of wind velocity and potential temperature under stably stratified conditions.

It is well known that the dynamic subgrid model have the capability to adapt different atmospheric condition and account for the grid size. Basu and Porté-Agel (2006) implemented a dynamic SGS model in MATLES code system to simulate GABLS1 case and showed reasonable results even with low resolution. Despite of the advanced dynamic model, current study put the focus on a static model. Deardorff subgrid model (Deardorff (1980)) being a common used subgrid model is built in many numerical models (list of models in Beare et al. (2006), Heus et al. (2010), Maronga et al. (2015), Gibbs and Fedorovich (2016)). However, the limitations and improvements of Deardorff subgrid model have been found over the years of research (Schumann (1991), Gibbs and Fedorovich (2016), de Roode et al. (2017)). Schumann (1991) argued that min operator used in the parameterizatoin of mixing length in Deardorff SGS TKE scheme should only be used for eddy diffusivity instead of eddy viscosity because the dissipation length scale increase with increasing shear. Gibbs and Fedorovich (2016) investigated several adjustments of Deardorff subgrid-scale model and proposed a modified scheme considering the dependence between the stability and eddy diffusivity. de Roode et al. (2017) presents an analytical solution of SGS TKE with the dependence on mixing length. Based on the observation of lower Prandtl number near the surface, de Roode et al. argued the existence of excessive mixing near the surface under Deardorff SGS model. Nonetheless, the sensitivity of grid size existing on the simulation of Deardroff SGS model is not solved by these inspections (Jiménez and Cuxart (2005), Beare et al.

(2006), de Roode et al. (2017), Maronga et al. (2020)).

In the current study, the sensitivity of grid size in SBL is addressed by identifying several fundamental issues of mixing length parameterization in Deardroff SGS TKE scheme (D80, Deardorff (1980)). A revised mixing length formulation is proposed to tackle these issues (named D80-R). To evaluate this new parameterization, a range of grid sizes are implemented in DALES code system (Heus et al. 2010) to simulate GABLS1 case. The simulation results are compared with the dynamic SGS model (MATLES, Basu and Porté-Agel (2006)). To further validate the new scheme, three different surface cooling rate cases based on GABLS1 are experimented to examine the effects of stability. To see the independence of LES code system, the simulation results from PALM code system with D80-R scheme are displayed. The sensitivity of numerical scheme and parameter prescribed in D80-R are explored.

This study have the following organization. The introduction is given in Chapter 1. In Chapter 2, the modified Deadroff SGS TKE scheme is proposed based on the introduction of large eddy simulation, description of subgrid models and investigation on mixing length scale. Followed by Chapter 3, the description of GABLS1 and setups of GABLS1 cases for evaluation of modified Deardorff SGS TKE scheme are detailed illustrated. The simulation results are demonstrated in Chapter 4. The model validation and discussion are also included. Finally, the conclusion and future perspectives are given in Chapter 5.

2

Large-eddy simulation

Large-eddy simulation as an advanced numerical technique developed for the representation of turbulence flow mainly in atmospheric and engineering field. The leverage of LES is that larger scale of motions are resolved on discretized grid and smaller motions are modelled using subgrid-scale model. A spectrum of popular used subgrid models is created and developed over the years with endeavor of accurate represention of the turbulent flow. The subgrid model from Deardorff (1980) is a popular and intensively used scheme. However, several fundamental issue are found with this Deardorff subgrid model. To handle this issue, a modified Deardorff subgrid model is introduced with a new parameterization of the mixing length formulation.

This chapter firstly introduces the large-eddy simulation by elaboration of various turbulent scales in atmosphere and the leverage of implementing LES using subgrid-scale model(Sect. 2.1). To parameterize the subgrid motions, Section 2.2 demonstrates the requirements and the different type of subgrid-scale models. The application of LES in stable boundary layer are discussed in Section 2.3. Lastly, the modified Deardorff SGS TKE is introduced by firstly the investigation of mixing length (Sect. 2.4).

2.1. Introduction to Large-eddy simulation

The history of turbulence can be traced back to Leonardo da Vinci (c. 1500) who attempted to sketch a diversity of turbulence flow and named them *turbolenza*. In the book *Weather Prediction by Numerical Process* (1922), Richardson described the processes of turbulence development as following:

> Big whorls have little whorls
> That feed on their velocity;
> And little whorls have lesser whorls
> And so on to viscosity

The concept of turbulence development in Richardson's perspective is that turbulence originates from large scale motions which are easy to break into relatively smaller scale eddies. The notion here called *energy cascade* will continue cascading successively for smaller eddies as well until the smaller eddies are small enough. Finally the small scale motions dissipates to heat. A visualization of multiple scales distribution of turbulence could be seen in Fig. 2.1 (figure taken from Schalkwijk et al. (2015)).

It was not until 1941 that Kolmogorov (1941) proposed a hypothesis that assumed the local isotropy of the small scale turbulence and its universal properties in sufficiently high Reynolds numbers flow. Based on this hypothesis, the relationship between length scale ℓ, velocity scale $u(\ell)$ and time scale $\tau(\ell) \equiv \ell/u(\ell)$ to describe turbulence could be revealed at various scale in Kolmogorov energy spectrum shown in upper panel of Fig. 2.2. The energy spectrum at sufficient large Reynolds number presents a variety of turbulence scale from largest integral scale l_0 to smallest Kolmogorov scale η. In other words, the large scale of motions generated by the planetary or mesoscale dynamics produces energy. Then the energy is transferring continuously as large size eddies twirl and rotate and shear to smaller scale

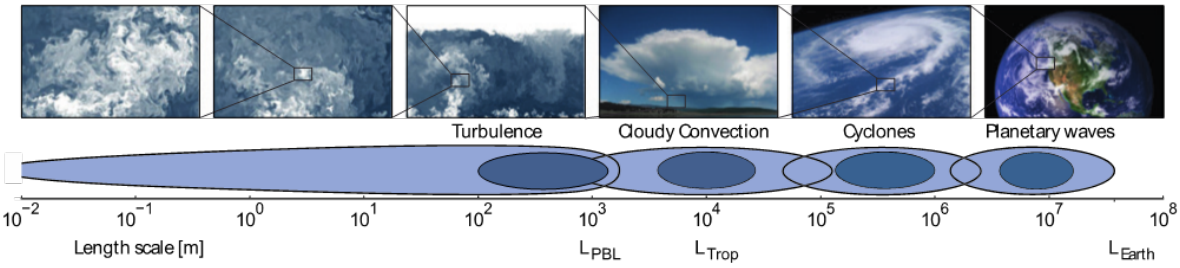

Figure 2.1: Multiple scales of turbulence in atmosphere (Schalkwijk et al. (2015))

eddies until eddies size reach around Kolmogorov scale η. The dissipation effect start to dominate and kinetic energy dissipate to heat by small scale viscosity.

Based on Kolmogorov's first similarity hypothesis, the small eddies within dissipation range have universal properties that are dependent on viscosity v and dissipation rate ε. The dimensional analysis of these two variable to describe length scale η, velocity scale u_η, and time scale τ_η in Kolmogorov scale gives:

$$\eta \equiv \left(v^3/\varepsilon\right)^{1/4} \tag{2.1}$$

$$u_\eta \equiv (\varepsilon v)^{1/4} \tag{2.2}$$

$$\tau_\eta \equiv (v/\varepsilon)^{1/2} \tag{2.3}$$

According to scaling from Kolmogorov scale to integral scale, dissipation rate at integral scale could be approximated as:

$$\varepsilon \sim u_0^3/\ell_0 \tag{2.4}$$

Combined equation 2.4 with Eq. 2.1, 2.2 and 2.3, the ratio between the smallest and largest scales could be determined as:

$$\ell_0/\eta \sim \mathrm{Re}^{3/4} \tag{2.5}$$

$$u_0/u_\eta \sim \mathrm{Re}^{1/4} \tag{2.6}$$

$$\tau_0/\tau_\eta \sim \mathrm{Re}^{1/2} \tag{2.7}$$

One who attempts to explicitly solve full scales in field e.g. a typical atmospheric layer would assume:

$$U_o \sim 7\ \mathrm{m\ s^{-1}}, \quad \ell_o \sim 10^3\ \mathrm{m}, \quad v \sim 1.5 * 10^{-5}\ \mathrm{m^2\ s^{-1}} \tag{2.8}$$

The kinematic viscosity value is taken under the condition of dry air at $20°$C and atmospheric pressure of 1000mb from (List et al. 1951, p. 395). The Reynolds number could be calculated:

$$\mathrm{Re} = \frac{U_o \ell_o}{v} \sim \frac{\left(7\mathrm{m\ s^{-1}}\right)\left(10^3\ \mathrm{m}\right)}{1.5 * 10^{-5}\ \mathrm{m^2\ s^{-1}}} \sim 4.67 * 10^8 \tag{2.9}$$

As a result, the ratio between integral scale to Kolmogorov scale and the Kolmogorov scale can be calculated:

$$\ell_0/\eta \sim 3.17 * 10^6, \quad \eta \sim 0.0003\ m \tag{2.10}$$

$$u_0/u_\eta \sim 1.47 * 10^2, \quad u_\eta \sim 0.0476\ \mathrm{m\ s^{-1}} \tag{2.11}$$

$$\tau_0/\tau_\eta \sim 2.16 * 10^4, \quad \tau_\eta \sim 0.0066\ s \tag{2.12}$$

In idealized case, totally around $3 * 10^{19}$ grid points in three dimensional space are required to fully explicitly represent this typical atmospheric layer, which far exceeds the capability of today's numerical computation. The method of fully resolving turbulence in all scales from Kolmogorov scale to integral scale is called Direct numerical simulation (DNS). The Navier-Stokes (N-S) equations have been considered as the standard physical formulation for description of the turbulence structure and properties. When DNS is applied to integrate the N–S equations, it consumes expensive computational resource and thus offers precise simulation dataset and fully detailed structure of the turbulence flow.

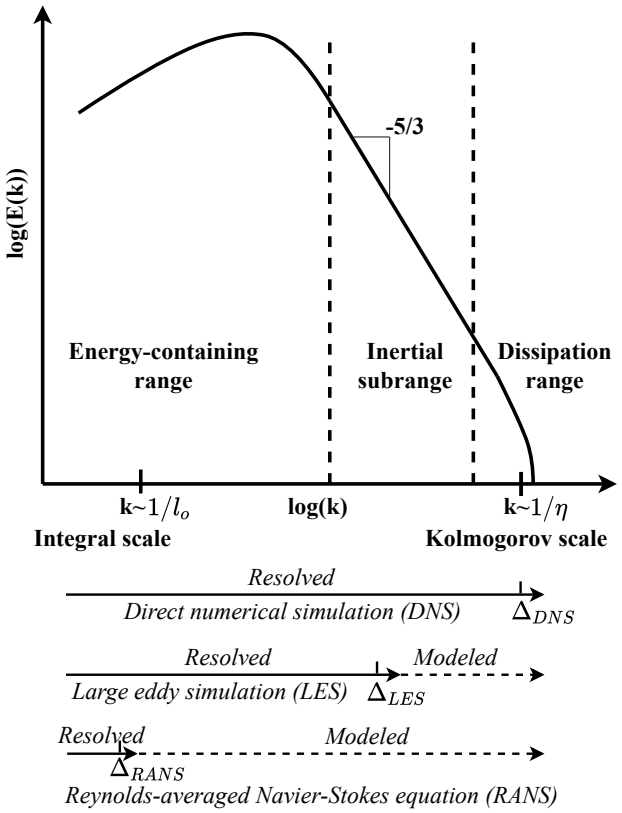

Figure 2.2: Kolmogorov energy spectrum at high Reynolds number (upper panel), where: k: wavenumber; E(k): the energy corresponding to wavenumber i.e. eddy size; l_0: integral scale; η: Kolmogorov scale. Different numerical method (bottom pannel), where Δ_{DNS}, Δ_{LES}, Δ_{RANS} are the scale resolved explicitly by each method respectively (This figure is adapted from (Geurts 2003, p. 59))

Frequently, DNS datasets are used for model validation, verification and improvement. Due to the expensive requirement of DNS, the workaround is to implement parameterization model within the numerical simulation. Reynolds-averaged Navier–Stokes equations (RANS) decomposes the variables in N-S equations into averaging part and fluctuation part. Then the Reynolds stress arose from treatment of Reynolds averaging is parameterized using turbulence closure models. The N-S equations under the Reynolds averaging operation results in a steady equations, which require less computational resources but only provide information of averaging statistics.

As a compromise between expensive DNS and simple RANS, large eddy simulation (LES) is a method that explicitly solves larger scale motions and parameterizes the small scale motions. Compared to averaging operation in RANS, spatial filter in LES is usually implemented with convolution operator for separation of high and low frequency motions. The motions left after the filter operation are called resolved turbulence and the small scale motion filtered out are called subgrid (SGS) turbulence.

The N-S equations derived from conservation law and Newton's law of motion (a full derivation could be seen in (Berselli et al. 2006, p. 32-35)) for incompressible flows are known as:

$$\frac{\partial u_i}{\partial t} + \frac{\partial \left(u_i u_j\right)}{\partial x_j} = -\frac{1}{\rho}\frac{\partial p}{\partial x_i} + v\frac{\partial^2 u_i}{\partial x_j \partial x_j} + \frac{g}{\theta_0}(\theta_{\mathrm{v}} - \theta_0)\delta_{i3} + F_i \tag{2.13}$$

Where u_i is the velocity in three dimension, t is the time, x_j is the spatial coordinate in three dimensions, ρ is the density, p is the pressure, v is kinematic viscosity, δ_{i3} is the Kronecker delta, F_i is other forcing terms. Each term in Equation 2.13 from left to right represent inertia, advection, pressure gradient force, viscous stress, buoyancy and other forcing respectively.

After the operation of spatial filter with width Δ_f, the equations turn to :

$$\frac{\partial \tilde{u}_i}{\partial t} + \frac{\partial \left(\tilde{u}_i \tilde{u}_j\right)}{\partial x_j} = -\frac{1}{\rho}\frac{\partial \tilde{p}}{\partial x_i} + \nu \frac{\partial^2 \tilde{u}_i}{\partial x_j \partial x_j} + \frac{g}{\theta_0}(\tilde{\theta_v} - \tilde{\theta_0})\delta_{i3} + \tilde{F_i} - \frac{\partial \tau_{ij}^R}{\partial x_j} \tag{2.14}$$

The tilde above each variable means the filtered variable after the operation of spatial convolution. The residual stress τ_{ij}^R as the product of spatial filter in Eq. 2.14 are usually parameterized in order to get closure of the N-S equation. Over the years, the research on a variety of such closure models called SGS models including eddy viscosity model, similarity model and dynamic model have been intensively explored, which will be elaborated in Section 2.2.

2.2. Subgrid Models

A proper subgrid (SGS) model has two basic requirements (Geurts 2003, p. 223). The first one is the energy transfer between resolved large scale motion and subfilter motions. The aim of subgrid models is to parameterize the high frequency motion part (small scale turbulence lower than filter width Δ_f) so that total resolved and modelled turbulence in LES are consistent with realistic nature or DNS simulation with high fidelity. In perspective of energy spectrum (Fig. 2.2), subgrid models serve as a bridge which have the function of energy transfer between the resolved motions and subgrid motions. The energy transferring from resolved turbulence to subgrid turbulence and its backscatter process should be well captured by ideal subgrid models. In this aspect, the difference between explicitly resolving the interaction of various scale of motions and the parameterization modelling lays in subgrid model bypassing the heavy integration of the partial differential equation by physical assumption of the dependency of the flow structure. The second requirement is that subgrid models should not be essentially affected by the filter width. As $1/\Delta_f$ stays in inertial range, the dynamic effect of subgrid model such as the interaction between motions should not be influenced by the filter width but the modelling subgrid stress is dependent on filter width to agree with overall results.

From theoretical point of view, one of the major concerns for subgrid modelling is physical and numerical interpretation of residual stress (SGS stress) term τ_{ij}^R. An clear derivation of how residual stress is decomposed into Leonard stress, cross stress and SGS Reynolds stress is shown in (Pope 2001, p. 583). The physical interpretation of each stress leads to various subgrid models discussed in following subsection. Specifically, D80-based and D80-R schemes are introduced in a detailed manner.

2.2.1. Eddy-viscosity models

The eddy-viscosity models are probably the most often implemented type of subgrid models in LES. Based on gradient hypothesis, the anisotropic residual-stress tensor τ_{ij}^{r} is assumed to depend on resolved strain rate tensor (Pope 2001, p. 581):

$$\tau_{ij}^{\mathrm{r}} = \tau_{ij}^{\mathrm{R}} - \frac{1}{3}\tau_{ii}^R \delta_{ij} = -2K_m \tilde{S}_{ij} \tag{2.15}$$

where:

τ_{ij}^{r} is anisotropic residual stress tensor

τ_{ij}^{R} is residual stress tensor

$\delta_{ij} = \begin{cases} 0 & \text{if } i \neq j \\ 1 & \text{if } i = j \end{cases}$

K_m is the eddy viscosity

$\tilde{S}_{ij}$ is the resolved rate of strain tensor

Based on dimensional analysis, the dimension of eddy viscosity K_m could be taken as multiplication of a length scale and velocity scale. The popular eddy viscosity models such as smagorinsky model and Deardorff SGS TKE scheme or the one would be proposed shall follow this dimension.

Smagorinsky model

Smagorinsky (1963) parameterized the eddy viscosity using a simple but popular formulation:

$$K_m = \left(C_s \Delta_f\right)^2 \ |\tilde{S}| \tag{2.16}$$

where C_s is smagorinsky coefficient, Δ_f is the filter width (in the context of DALES implicitly equals to grid size) and the characteristic resolved strain tensor $|\tilde{S}| = \left(2\tilde{S}_{ij}\tilde{S}_{ij}\right)^{1/2}$. The mixing length is defined as $C_s\Delta_f$. The C_s varies based on different condition to account for averaging energy transfer between various flow structures. In DALES, C_s is set as constant 0.22. It does not consider the backscatter process within this model. In the condition of shear dominated flow, the C_s is changed to 0.1 (Geurts and Fröhlich (2002)) to avoid excessive dissipation.

Deardorff SGS TKE scheme

In terms of Deardorff SGS TKE scheme (D80, Deardorff (1980)), K_m is parameterized by adding one extra physical equation of subgrid turbulent kinetic energy e, which is so called one-equation eddy viscosity subgrid model. In the context of DALES, the prognostic equation of e is given as:

$$\frac{\partial e}{\partial t} = -\frac{\partial \tilde{u}_j e}{\partial x_j} - \tau_{ij}\frac{\partial \tilde{u}_i}{\partial x_j} + \frac{g}{\theta_0}R_{w,\theta_v} - \frac{\partial R_{u_j,e}}{\partial x_j} - \frac{1}{\rho_0}\frac{\partial R_{u_j,\pi}}{\partial x_j} - \varepsilon \tag{2.17}$$

where the terms from left to right mean the effect on SGS-TKE by either production or destruction: storage, advection, shear, buoyancy, transport of SFS stress, pressure transport and dissipation. (See how each term is parameterized in Deardorff (1980) and Heus et al. (2010)).

Following Deardorff (1980), the eddy viscosity for momentum, eddy diffusivity for heat and scalar and energy dissipation rate are parameterized as:

$$K_{\mathrm{m}} = c_{\mathrm{m}}\lambda e^{1/2} \tag{2.18}$$

$$K_{\mathrm{h}} = c_{\mathrm{h}}\lambda e^{1/2} \tag{2.19}$$

$$\varepsilon = \frac{c_\varepsilon}{\lambda}e^{3/2} \tag{2.20}$$

These three key terms are highly dependent on mixing length scale λ and e. The mixing length is parameterized using Eq. 2.21. (please note that this parameterization in DALES system is activated only when option *ldelta* is set to .false. otherwise $\lambda = \Delta$ is used)

$$\lambda = \min(\Delta, L_b) \tag{2.21}$$

where Δ is grid size which is directly taken as mixing length originally in Lilly (1966) study and L_b is the buoyancy length scale brought to represent smaller length scale under stratification condition in the intention of Deardorff. It is defined as:

$$L_b = c_N\frac{e^{1/2}}{N} \tag{2.22}$$

where C_N equals to 0.76 and N is Brunt-Väisälä frequency which is formulated as:

$$N^2 = \left[\frac{g}{\theta_0}\frac{\partial \tilde{\theta}_{\mathrm{v}}}{\partial z}\right] \tag{2.23}$$

Where, g is gravitational constant. The θ_0 and $\tilde{\theta}_{\mathrm{v}}$ are reference potential temperature and resolved virtual potential temperature. L_b depends on both stratification and e.

The parameter c_m is prescribed as 0.117 and the c_h and c_ϵ in Equations (2.19) and (2.20) are related to grid size and mixing length as:

$$c_h = \left(1 + 2\frac{\lambda}{\Delta}\right)c_m \tag{2.24}$$

$$c_\varepsilon = 0.19 + 0.51\frac{\lambda}{\Delta} \tag{2.25}$$

The SGS Prandtl number is formulated as:

$$\mathrm{Pr}_{\mathrm{s}} = K_{\mathrm{m}}/K_{\mathrm{h}} = c_m/c_h \tag{2.26}$$

As there is one extra physical equation used in modelling system, the results should be more realistic than simple smagorinsky model and at the same time the computational cost becomes heavy.

2.2.2. Other SGS models

Similarity models

The similarity model is based on that the subgrid stress close to filter width with highest frequencies could extrapolate to another subgrid stress with lower frequency. In other words, the turbulence structure under two different filter width have similarity. However, the turbulence stress is often underestimated (Geurts 2003, p. 229).

Stochastic models

What stochastic models approach the subgrid modelling is by including a random forcing term into momentum equations. This random forcing term will incorporate the function of energy backscatter process which is not captured in eddy viscosity model. However, this model does not reflect the correlations of statistic between subgrid turbulent motions (Sagaut 2006, p. 178).

Dynamic models

In terms of eddy viscosity subgrid model, one of the major concerns is that the constant smagorinsky coefficient or C_m in D80 scheme can only suit for specific type of flow. Furthermore, the constant coefficient is applied in 3 dimensional field over time, which often does not account for the effect of presence of surface. Fortunately, Germano et al. (1991) proposed a dynamic model which calculates the model coefficient instantaneously based algebraic identity (also called Germano identity) between two different filtered fields. Based on this model, the point-wise coefficient can be determined based on local information and adapt to various flow condition. Later in Lilly (1992), an improvement of Germano's dynamic model which includes a least squares calculation to minimize the error was made. However, the local eddy viscosity may instantaneously show negative values and it is often handled with averaging operation over one direction. This averaging treatment may not be suitable for complex flow. To solve this problem, Meneveau et al. (1996) proposed a Lagrangian averaging technique which accumulates the information over the pathline of flow. Porté-Agel et al. (2000) proposed a scale dependent dynamic model for simulation of neutral boundary layer. In the study of Basu and Porté-Agel (2006), a new scale-dependent tuning-free subgrid model which calculates the smagorinsky coefficient and Prandtl number locally for stable boundary layer is proposed.

2.3. LES of stable boundary layer

In the context of diurnal cycle and thermal-dynamic turbulent structure, atmospheric boundary layer (ABL) is categorized into three types of stability layer: convective boundary layer (CBL), neutral boundary layer (NBL) and stable boundary layer (SBL). CBL often occurring during day-time is driven large scale mixing by dominant buoyancy and shear mechanism. In contrast, SBL with stably stratification often forms with surface cooling during night time or in polar regions. The development of turbulence in SBL is controlled by the balance between shear and negative buoyancy force, which leads to smaller turbulence structure. Therefore, the progress of understanding SBL have long been hampered compared to CBL because of its inherent small-scale eddy motions, the limitation of computational resources, the lack of physical and robust parameterization of numerical model, the understanding of strong sensitivity of turbulent structure with complex scenarios (e.g., heterogeneous surface, complex terrain, intermittency).

Despite of these difficulties, the progress of understanding SBL by employing LES model have been promoted with enthusiasm regarding the essential role of representation of SBL in weather prediction models and its applications in various fields (e.g., wind energy, air quality; Park et al. (2014)). The first LES simulation of stable boundary layer is completed in Mason and Derbyshire (1990). In this study, an idealized and homogeneous stable boundary layer is simulated using a Smagorinsky SGS model with stability function R_f and the results are in agreement with local scaling hypothesis from Nieuwstadt (1984). Thereafter, a variety of studies have been conducted to improve the simulation results in Mason and Derbyshire (1990) and the results from most of them followed local scaling hypothesis (Nieuwstadt (1984)). To deal with the excessive shear near the surface shown in Mason and Derbyshire (1990), Brown et al. (1994) adapted a stochastic subgrid model from Mason and Thomson (1992) to enhance the dependence of stability and account for backscatter process. The agreement between the non-dimensional shear, temperature gradient and surface observations improved because of representation of backscatter effect. In contrast, Andren (1995) investigated the turbulent structure near the surface

by a comparison between a original SGS TKE model and a two-part eddy viscosity model. The two-part eddy viscosity model including a random forcing in SGS stress improved the simulated results especially near the surface and allowed the agreement with local scaling hypothesis. Compared with simulated data in Andren (1995), Galmarini (1998) implemented two LES model and a one-dimensional model and results showed agreement with experiment data and local scaling hypothesis.

The capability of LES to produce the mean profiles and other statistics of turbulent structure in SBL have shown promise in abovementioned studies. This progress accelerates with introduction of observational studies (CASE-99, Poulos et al. (2002); SHEBA, Persson et al. (2002)) and model intercomparison (Beare et al. (2006), Basu et al. (2012)). A comprehensive and relatively realistic stably stratified boundary layer is explored in Kosović and Curry (2000). The LES in this study with a nonlinear SGS model is driven by the initial condition and boundary condition from observation data in Beaufort Sea Arctic Stratus Experiment (BASE). To better understand the evolution of turbulence under different stably stratified condition, the parameters such as geostrophic wind, surface cooing rate, inversion strength and roughness length are experimented. Based on the exploration of different atmospheric condition, GABLS1 case was identified as an idealized moderate stably stratified condition for intercomparison study of LES. The progress and understanding based on GABLS1 case are detailed discussed in Sect. 3.1.

2.4. Modified SGS TKE Scheme

In current study, several fundamental problems are identified in the parameterization of mixing length within original Deardorff SGS TKE (D80) scheme under stably stratified condition. Before the introduction of new proposed mixing length formulation (Sect. 2.4.2), the research of mixing length scale is reviewed in Sect. 2.4.1.

2.4.1. The mixing length scale

The mixing length theory was firstly proposed in Prandtl (1925) with the aim of modelling eddy viscosity by a theoretical formula that could be easily tested by experiment. The eddy viscosity was expressed by Prandtl as following (the consistent variable notation are set):

$$K_m = \lambda \cdot \lambda \left| \frac{dU}{dy} \right| \tag{2.27}$$

where λ is mixing length and the momentum exchange of turbulent flow is reflected by the term $\lambda \left| \frac{dU}{dy} \right|$. Here, Prandtl considered the mixing length variable as "*the travelling length of a particle until the particle mixed with ambient flow*" or "*the diameter of the fluid motion*". Further statements from Prandtl argued the unknown quantity transferring from eddy viscosity to mixing length could adjust to specific type of flow only based on length scale dimension. Prandtl admitted the mixing length formula requires complex interpretation to account for various condition such as presence of surface. (Bradshaw (1974); (Davidson et al. 2011, p. 55)).

To account for the presence of surface, Von Kármán (1930) proposed the mixing length formula as:

$$\lambda = \kappa U'/U'' \tag{2.28}$$

where U' and U'' are the first and second derivatives of velocity respectively. κ is *von Kármán constant*. This formula explicitly solved the mixing length based on local information of shear and allowed the logarithmic distribution of velocity near the surface (Davidson et al. 2011, p. 58).

In the study of Blackadar (1962), the eddy viscosity is parameterized using mixing length and energy dissipation rate instead of wind shear under neutral condition as:

$$K_m = \epsilon^{1/3} \lambda^{4/3} \tag{2.29}$$

where ϵ is energy dissipation rate which is calculated in Blackadar (1962) as:

$$\epsilon = K_m \left[\left(\frac{dU}{dz} \right)^2 + \left(\frac{dV}{dz} \right)^2 \right] = K_m S^2 \tag{2.30}$$

The combination of eqs. (2.29) and (2.30) surprisingly leads to Eq. 2.27. In their model, the mixing length near the surface is set to κz term. With the consideration of Von Kármán (1930)'s formulation and analysis of Leipzig wind profile, a new mixing length formula was proposed as following (the variable notation have been changed for consistency of current study):

$$\frac{1}{\lambda} = \frac{1}{\kappa z} + \frac{1}{l_0} \tag{2.31}$$

where l_0 is the parameter will take over λ when the height reaches to free atmosphere and it is parameterized related to geostrophic wind and coriolis parameter. One note here is that mixing length formula in Blackadar (1962) is to simulate wind distribution under neutral condition.

Subsequently, the application of mixing length started to flourish and a spectrum of mixing length formulas confirmed Prandtl's insights on the requirement of complex form. In a later study of Lacser and Arya (1986), a comprehensive summary of mixing length formulations was presented and these formulas were tested using one dimensional model with TKE closure under neutral boundary layer. Most of these formulations adapted from Blackadar's equation (Eq. 2.31) attempted to parameterize l_0 or add extra term to account for stability. One of them from Brost and Wyngaard (1978) used a similar buoyancy length scale l_b to account for stability and z as the limits of the wall. Andre et al. (1978) followed a minimum function between a buoyancy length scale (with e) and Blackadar length scale. In the context of three-dimensional large-eddy simulation, Smagorinsky (1963) and Deardorff (1980) implemented mixing length scale within their subgrid model to account for the interaction and energy transferring processes between the resolved motions and SGS motions (described in section 2.2.1). There are extensive research on new mixing length parameterizations under neutral condition (Peña et al. (2010)), stable condition (Table III in Cuxart et al. (2006)); LES models in Beare et al. (2006)).

The interpretation of mixing length has grown with some comprehensive comparison studies (Lacser and Arya (1986), Cuxart et al. (2006), Peña et al. (2010)) and various testing conditions (Sullivan et al. (2016), Rodier et al. (2017), Huang and Bou-Zeid (2013)). However, it is found that one robust and effective mixing length parameterization for various complex scenarios is quite challenging. To aim this end, several necessary elements of mixing length are found based on these studies.

- The first one is the dependence between the mixing length and filter width (the grid size in implicit filter or ratio of grid size in explicit filter) for SGS effect (Lilly (1966)). As the filter width changes, the turbulence stress parameterized by mixing length should be related.

- The second one is the presence of surface. Starting from κz term implemented in Blackadar (1962), z term in Brost and Wyngaard (1978) and $c_n \kappa z$ ($c_n = 0.516$) in Baas et al. (2008), Deardorff (1980) increased the dissipation parameter c_ϵ in eq. (2.25) to a large value to avoid unduly large TKE because of small dissipation rate close to the surface. The κz term showed robustness not only in neutral condition (Peña et al. (2010)) but also stable condition (Cuxart et al. (2006)) since Blackadar (1962) tested it under neutral condition. The von karman constant proved to produce logarithmic velocity distribution near the surface (Peña et al. (2010) and (Davidson et al. 2011, p. 58)).

- The stability dependence might be a complex element to represent due to the lack of understanding of turbulence structure under various stability conditions. Under unstable convective condition, the turbulence mixing are much intense and the mixing length are much larger. Under neutral condition, other factors such as presence of surface and geostrophic wind come into play. Under stable condition, vertical stratification lead to limitation on turbulence transport. As a result, the mixing length is much smaller than in convective condition. Many combinations including stability function in parameterization of eddy viscosity are used to represent different stability effect. Cuxart et al. (2006) showed a list of single column model (SCM) using stability function with dependence of Richardson number $f_m(Ri)$. Furthermore, buoyancy length scale related to TKE and buoyancy frequency in Deardorff (1980), the Lagrangian form length scale related to local Obukhov length used in Degrazia et al. (1996), the combination of shear and buoyancy length scale in Rodier et al. (2017) and the appropriate Shear length scale for stable boundary layer condition (Basu et al. (2020)) are investigated.

2.4.2. Modified SGS TKE scheme

In this section, the modified Deardorff SGS TKE scheme (D80-R) is introduced based on the diagnosis of Deardorff SGS TKE scheme (D80) and understanding of mixing length. Several fundamental problems identified in D80 later are proved in results section leading to grid sensitivity issue under stable boundary layer. To tackle this issue, a inverse linear interpolation between neutral length scale κz and buoyancy length scale L_b (Eq. 2.22) for parameterization of mixing length is proposed.

According to the description of D80 scheme in Section 2.2.1, K_m, K_h and ϵ are highly dependent on mixing length scale λ which is parameterized in Eq. 2.21. Under neutral condition, K_m, K_h and ϵ are only dependent on Δ and e. The parameters c_m, c_h (Eq. 2.24) and c_ϵ (Eq. 2.25) are constant and Pr_s equals 0.33 under this condition. In very stable condition, with $1/N$ approaching 0 (Eq. 2.23), λ equals to L_b approaching 0 and Pr_s equals to 1. Under stably stratified condition, the stability dependence of these terms are mainly through the buoyancy length scale L_b. However, under stably stratified condition, if typical value of temperature gradient $0.01 Km^{-1}$, e taken as $0.1 m^2 s^{-2}$ and reference temperature 263.5K are used (from initial condition of GABLS1 in Sect. 3.1), the bouyancy length scale in stable condition results in around 10m in the lower part of boundary layer. As mentioned in section 2.3, it is common practice to implement fine resolution lower than 5m to resolve small turbulence structure (Beare et al. (2006)). Especially in Sullivan et al. (2016), a range of grid size (0.39m, 0.78m and 2m) are utilized to experiment the grid sensitivity issue. As a direct consequence, the mixing length λ will be dominant by small value of Δ very often in the lower or middle part of SBL depending on the stability length scale. Then the generation of turbulence depending on instantaneous variable of K_m, K_h and ϵ will diminish to a large extent. The modified formulation of mixing length adapt from Blackadar (1962) and Brost and Wyngaard (1978) applies a inverse linear interpolation between κz and buoyancy length scale L_b in Eq. 2.22. Near the surface, κz term is smaller than L_b which leads to influential role of presence of surface by κz because of the inverse operator. As the height goes up, κz linearly increases to a larger number and the bouyancy length scale start to contribute to mixing length scale as would be physically expected. The advantage of this operator is that the transition between κz and L_b is smooth than *min* operator.

$$\frac{1}{\lambda} = \frac{1}{\kappa z} + \frac{1}{L_b} \tag{2.32}$$

This revised formulation of mixing length theoretically progressed in three aspect. It avoids the dominant role of grid spacing by substitute the Δ with κz when fine resolution are required for stable boundary simulation. Concurrently, the presence of surface is considered by the small value of κz near the surface. When the height goes higher, κz term takes less contribution in λ as the physical surface would reveal. At the same time, the buoyancy length scale near the surface should be limited by the small value of κz due to presence of the surface. Then the buoyancy length scale starts to contribute as the turbulence flow leaves the surface (Van de Wiel et al. (2008)). In the case of D80 scheme, the stability dependence based on L_b would be limited if the used resolution is smaller than L_b. In contrast, D80-R SGS model eliminates this limitation. The third one is the modification of $min\{\}$ operator to inverse linear interpolation, which optimizes the smooth transition from κz to buoyancy length scale L_b. However, the substitution of Δ with κz reduces the dependency of mixing length on filter width (implicitly on grid size). The effect of grid-size in D80-R scheme is felt by c_h and c_ϵ. The evaluation of D80-R in terms of simulation results are presented in Chapter 4.

2.5. Summary

In this chapter, the new parameterization of mixing length in D80-R is proposed to substituted the original D80 scheme with the consideration of three elements of mixing length. The representation of surface using κz considers the effects of a wall on eddy size and also avoids the issue of cutting off by Δ. The buoyancy length scale takes contribution to stability effects and the grid-size dependence is implicitly felt through parameter c_h and c_ϵ.

3

Description of the simulation

In current study, GABLS1 case as an idealized moderate stable condition is taken as the test field and the Dutch Atmospheric Large-eddy Simulation (DALES; Heus et al. (2010)) system is mainly implemented for the new proposed mixing length formulation in Deardorff SGS TKE scheme. In addition to test the modification in D80-R is independent of specific code system, the simulation dataset of GABLS1-LES from PALM model (Maronga et al. (2015)) is presented and compared. To further examine the performance of D80-R under higher stability condition, stronger surface cooling rate of GABLS1 cases are simulated. For comparison, the dataset from MATLES model (Basu and Porté-Agel (2006)) which use scale dependent dynamic SGS model (LASDD) are laid out in all testing case. To explain the details of all experiment settings, the organization of this chapter is as following. The research footprint of GABLS1 are described in section 3.1. The description of setups of GABLS1 and extension of GABLS1 cases are presented in section 3.2. To summary all the experiments, Table 3.1 in Section 3.3 is presented.

3.1. GABLS1

Within the program of Global Energy and Water Cycle Experiment (GEWEX), the GEWEX atmospheric boundary layer study (GABLS) initiated by Holtslag (2003) mainly aims at comprehensive understanding of atmospheric boundary layer and its representation in numerical models especially the focus on stable boundary layer. To aim this end, the first intercomparison of Large-eddy simulation model under stable condition in Beare et al. (2006) and single column model (SCM) in Cuxart et al. (2006) are launched. Beare et al. (2006) involved eleven participants with different SGS models and provided various aspects of comparison such as grid sensitivity and SGS model sensitivity. Despite the difficulties of representing stable boundary layers discussed in section 2.3, Beare et al. (2006) showed the consistent results from most of the LES models and thus can be taken as the benchmark (Holtslag et al. (2013)) for evaluation of numerical model including new parameterization of SGS model or weather prediction model. In addition, the valuable insights from GABLS1 promoted a better understanding of turbulence structure under stable condition.

The advent of LES intercomparison based on GABLS1 case in Beare et al. (2006) connected the preceding and following research on representation of stable boundary layer. Before the intercomparison of large eddy simulation in Beare et al. (2006), the progress of LES in SBL have been long lagging due to the lack of understanding of stable boundary layer and limited computational power. There are only some studies have been reported (discussed in Sect. 2.3). It is 16 years since the first comprehensive LES-SBL by Mason and Derbyshire (1990) that the development of LES-SBL have slowly progressed as the computational power increases. The endeavor of better numerical simulations of stable boundary layer meet with the initialization of GABLS1 case which is based on an comprehensive investigation of various conditions in Kosović and Curry (2000).

Over the years, the framework of LES under stably stratified condition have grown increasingly in aspects of better SGS model, surface layer representation and complex scenarios since the intercomparison study in Beare et al. (2006) was launched. Some insights on turbulence structure and numerical representation have been gained from GABLS1 and extent to more complex scenarios. Jiménez and

Cuxart (2006) analyzed the high resolution GABLS1 dateset using probability density function to get insights on the relationship between the turbulence structure and statistics. Kitamura (2010) compared four SGS models based on the test field of GABLS1 to evaluate the vertical flux and concluded the overestimation results from the deardorff SGS TKE scheme at coarser resolution. Huang and Bou-Zeid (2013) investigated the turbulence structure under different surface cooling rate cases based on GABLS1 with double horizontal domain size. In comparison, Sullivan et al. (2016) investigated turbulence structure under a range of cooling rate cases and different grid spacing based on GABLS1 case.

Holtslag (2006) analyzed the problem of enhanced mixing thus leading to deeper boundary layer in weather prediction model. The attention of presence of surface layer coupled in LES model has been drawn in the study of Steeneveld et al. (2006) which addressed the enhanced mixing due to misrepresentation of surface boundary condition. With the consideration of surface energy budget, Steeneveld et al. compared the methods of surface energy balance and bulk conductance layer. Both methods lead to shallower boundary layer and stronger surface cooling. Basu et al. (2008) using a analytical approach proved that surface boundary condition prescribed by temperature gives more realistic results than surface sensible flux under moderate to very stable condition. In the study of Svensson and Holtslag (2009), furthermore, the relationship between the surface wind angle, surface stress and boundary layer height is examined based on GABLS1 dataset and some model simulations. The role of first grid level is of great importance to give better representation of surface flux. The new parameterization of stable boundary layer height proposed in Steeneveld et al. (2007) based surface friction velocity, surface bouyancy flux, coriolis parameter and stability parameter N is consequently affected by first grid height. However, Maronga et al. (2020) proposed an elevated grid point used in Monin–Obukhov Similarity Theory for the calculation of surface flux. This modification might avoid the dilemma of choosing the vertical resolution and the violation of MOST (Basu and Lacser (2017)).

In terms of complexity of surface, the heterogeneity of surface under stable stratified condition are experimented in Stoll and Porté-Agel (2009), Miller and Stoll (2013) and Mironov and Sullivan (2016). To get better understanding of more realistic scenario of heterogeneous surface boundary condition of the temperature, Stoll and Porté-Agel (2009) implemented dynamic subgrid model to simulate a range of adapted the GABLS1 cases of which the surface cooling rate are arranged in different patches. In comparison, Miller and Stoll (2013) studied the heterogeneity of surface roughness in stably stratified condition using a series of Large eddy simulation based on GABLS1. Futhermore, Sterk et al. (2013) considered about the small scale processes including the presence of snow surface and radiation in stable stratified condition based on adaptation of GABLS1 case. Similar to Stoll and Porté-Agel (2009), Mironov and Sullivan (2016) investigated the heterogeneity of the surface temperature depending on the length in streamwise direction with revison of GABLS1 case.

The GABLS1 case as a golden benchmark for LES-SBL study shows great promises in validation of numerical model and understanding of turbulent structure. First of all, the capability of GABLS1 as validation experiment in simulating stable boundary layer has been shown in several large eddy simulation model (MATLES, Basu and Porté-Agel (2006); DALES, Heus et al. (2010); PALM, Maronga et al. (2015)); MicroHH, van Heerwaarden et al. (2017). Moreover, Enriquez and Street (2014) proposed a linear algebraic subgrid-scale model that assumes the SGS stress could be expressed using linear functions. This model is validated using a case with changing surface cooling rate over time based on GABLS1 case. Lu and Porté-Agel (2014) evaluated a dynamic SGS closure model under neutral and stable condition. GABLS1 case is adapted with double horiozntal domain size for testing the stable condition. The result are in agreement with Basu and Porté-Agel (2006) and show less grid sensitivity. In the study of Matheou and Chung (2014), a new stretched-vortex subgrid model is proposed to simulate the atmospheric boundary layer in various stability cases and a range of grid size. To test the stable condition, GABLS1 case is simulated and the results are in the range of previous simulations in Beare et al. (2006). In comparison, The simulation of convective boundary layer and stable boundary layer are evaluated using a minimum dissipation model for subgrid flux in Abkar and Moin (2017). The GABLS1 case is again simulated here with double horizontal domain compared to Beare et al. (2006). The simulation results show little sensitivity to grid spacing and good agreement to local scaling hypothesis (Nieuwstadt (1984)).

More than large eddy simulation, the performance of single column model under stable condition developed with rapid speed based on GABLS1 case. Rodrigo and Anderson (2013) proposed a flux-profile SCM based on local scaling hypothesis and validated the model using GABLS1 case. The

local scaling hypothesis that describes the turbulence structure of entire atmospheric boundary layer originated from Nieuwstadt (1984) and examined in Basu et al. (2006) and van Dop and Axelsen (2007). Based on this hypothesis, Donda et al. (2013) adopt a standard SCM with a turbulence closure and examined using GABLS1 case. Furthermore, Zbigniew Sorbjan investigated the turbulence structure under stable condition based on a K-theory model in Sorbjan (2012) and Sorbjan (2014). In terms of the complex scenarios, the transition of diurnal cycle from SBL to CBL is investigated by firstly applying a explicit algebraic turbulence model to simulating the GABLS1 case in Lazeroms et al. (2016). In Ďurán et al. (2018), a modified SGS TKE scheme in SCM is presented to simulated various condition including convective boundary layer, stable boundary layer (GABLS1) and moist condition. The coupling between mesoscale model and LES is inspected based on GABLS1 in Muñoz-Esparza et al. (2014) and Udina et al. (2016).

Within the subgrid parameterization, mixing length scale is a crucial variable which is detailed in section 2.4.1. Based on simulations on GABLS1 case, shear length scale is proved to give more realistic results than buoyancy length scale in Buzzi et al. (2011), Wilson and Venayagamoorthy (2015), Rodier et al. (2017). In summary, various parameterizations of mixing length or numerical model elaborated above are mainly validated by GABLS1 or extension of GABLS1 case which further proved its fidelity, popularity and quality being golden benchmark. Furthermore, GABLS1 case can also provide insight to many applications such as wind energy (Porté-Agel et al. (2010); Lu and Porté-Agel (2011); Porté-Agel et al. (2013); Bhaganagar and Debnath (2015); Rodrigo et al. (2017); Xie and Archer (2017)) and particle dispersion (Steinfeld et al. (2008)).

3.2. Cases setup

This section demonstrates the prescription of GABLS1 and the steps of setup GABLS1 as basic testing case in DALES system. The prescription of GABLS1 in current study is following Beare et al. (2006). The initial condition have a mixing layer of 265K potential temperature in the lower 100m region (Fig. 3.1). On top of that, it is inversion layer with intensity of $0.01 Km^{-1}$. The initial wind speed profile follows constant geostrophic wind speed of 8 ms^{-1} with the direction in east-west (Please note the surface wind velocity is zero). In the context of SGS TKE scheme, the initial condition of the turbulent kinetic energy is prescribed using equation $0.4(1 - z/250)^3 \mathrm{m}^2\mathrm{s}^{-2}$ for the height below 250m. Above that height, the initial value of SGS TKE equals to zero.

The surface boundary condition is prescribed using three surface cooling rate = (0.25 K/h, 0.50 K/h, 1.00 K/h) for 9 hours to reach stably stratified condition. In addition, the coriolis parameter is $1.39 \times 10^{-4} s^{-1}$ (latitude 73°N). The surface roughness length z_0 for momentum and scalar are assumed to be 0.1m which follows the prescription in Beare et al. (2006). To allow the turbulence to generate at initial time of simulation, there is random perturbation of potential temperature in the lower 50m with the standard deviation of 0.1K and zero mean.

Based on the atmospheric condition prescribed above, the environment of all LES models are set with a domain size of 400m × 400m × 400m. To test the aforementioned grid size sensitivity issue, a wide range of isotropic grid spacing Δ = (12.5m, 10m, 8m, 6.25m, 5m, 4m, 3.125m, 2m) correspond-

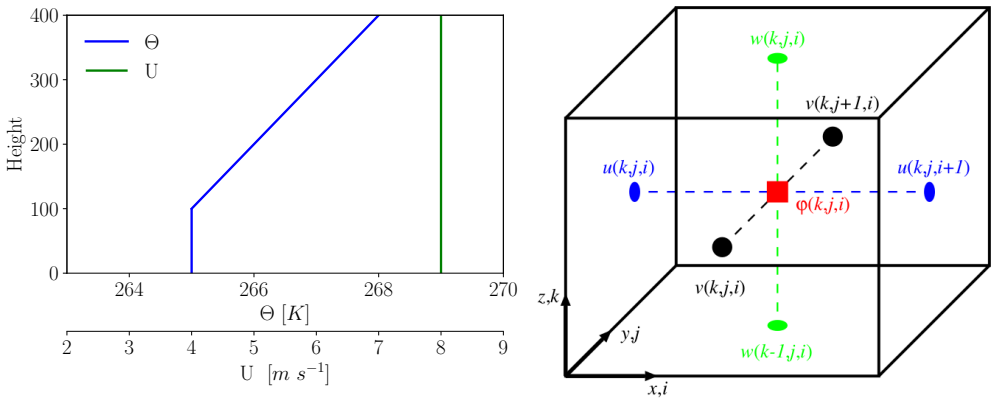

Figure 3.1: Left: the initial condition of potential temperature profile (blue line) and wind velocity profile (green line). Right: An Arakawa C-grid (Maronga et al. (2015))

ing to grid points of $(32^3, 40^3, 50^3, 64^3, 80^3, 100^3, 128^3, 200^3)$ in three dimension are implemented. The setup processes of how the 6.25 m resolution case with surface cooling rate of 0.25k/h as an example is detailed illustrated with description of *namoptions* file in appendix A. Following these steps, all the simulations with different grid size could be set up by simply changing the grid number in three dimension in DALES system. In comparison, the simulation results from a locally averaged scale-dependent dynamic subgrid model in MATLES code system (LASDD; Basu and Porté-Agel (2006)) is taken as a benchmark in the current study. The grid size used in LASDD is 3.5 m.

In terms of the numerical scheme applied in models, the domain is discretized with a staggered grid with the arrangement type of an Arakawa C-grid shown in Fig. 3.1. To numerically solve the partial differential equation for various variables (scalars and vectors), DALES and PALM code system apply finite-difference method and MATLES code uses pseudo-spectral method. For the dynamic code MATLES, a 2nd order Adams-Bashforth scheme is utilized. DALES and PALM code both use a 3rd order Runge-Kutta scheme along with a 5th order advection scheme in the horizontal direction (Wicker and Skamarock (2002)). As for vertical direction, DALES have a 2nd order scheme and a 5th order scheme is used by PALM.

The time steps Δt for integration in DALES equals to constant 0.1 s to avoid discretization error in temporal space. However, the simulations from PALM model use an adaptive time step and LASDD model have a fixed time step of 0.075 s. In this study, the total simulation time of 9 hours as most of the models running in Beare et al. (2006) is set to reach the quasi-equilibrium state. Following the prescription by MacVean (2003), the statistics sampling interval of the simulations is set as 1 min and the output is written with interval of 5 minutes.

The treatment of surface condition in DALES and PALM code follows Monin-Obukhov similarity theory (MOST), the processes of which include the flux parameterization along with iterative calculation of Obukhov length L using prescribed surface wind speed and temperature. However, the first grid height should not be in roughness sublayer (height ~ $50z_0$) (Basu and Lacser (2017)). In current study, this precondition might be violated for the experiments of grid size finer than 5m. However, these fine resolution cases are still included for investigation. Moreover, the effect of violation is not noticeable under current experiment condition even with grid size finer to 2m and it is unknown why this is the case in the current study.

One addition note is that the only difference between the D80-based scheme and D80-R scheme is the formulation of mixing length. The parameter and other formulation in SGS scheme keep intact as the original model for both DALES and PALM. There are slightly differences between DALES code system and PALM code system. In default D80 scheme, a different formula of mixing length is prescribed by PALM ($\lambda = min(1.8z, \Delta, L_b)$) under stable condition. In D80-R scheme, c_h equals to c_m. In addition, The prescribe parameter c_m equals to 0.12 and 0.1 for DALES code and PALM code respectively.

3.3. Summary

This chapter displays a thorough description of setting up the GABLS1 cases for testing the D80-R scheme regarding the essential role of GABLS1 case in understanding the turbulent structure and validation with high fidelity data. The comprehensive testings (shown in Table 3.1) of D80-R include the simulations of GABLS1 using a range of grid size, varying stability of GABLS1 and code system independence. Later, validation section includes the sensitivity of numerical scheme and c_m parameter (discussed in Sect. 4.3.1).

Table 3.1: The summary of the experiments. In terms of resolution cases, ALL means Δ = (12.5m, 10m, 8m, 6.25m, 5m, 4m, 3.125m, 2m) and ALL* means PALM code system run a extra case of Δ = 1m. In terms of participated code system, the shown code system corresponds to the overlaid lines in the results section (Sect. 4.1)

Experiment	Resolution cases	Participated code system	Surface cooling rate
Stability	ALL	DALES, MATLES	(0.25K/h, 0.50K/h, 1.00K/h)
Code system independence	ALL*	DALES, PALM, MATLES	0.25K/h
Sensitivity of advection scheme	6.25m	DALES	0.25K/h
Sensitivity of parameter c_m	6.25m	DALES	0.25K/h

4

Results and Discussion

In order to evaluate the performance of modified Deardorff SGS scheme (D80-R), the statistical descriptions of turbulence flow from different stability cases of GABLS1 are presented in this chapter. These statistical analysis are categorized into three sections: Time series section (Sect. 4.1.1), First order (Sect. 4.1.2) and second-order statistics (Sect. 4.1.3). Based on the characteristics depicted from these statistical analysis, it is followed by additional analyses section (Sect. 4.3) which addresses the sensitivity of the advection scheme and prescribed parameter in D80-R. The simulation results from PALM model is included in appendix B to demonstrate the independence of LES code system.

4.1. The statistical results

To specify the layout of following figures in advance, the vertical profiles of the mixing length taken as an example shown in Fig. 4.1 are planar averaging and temporal mean profile in the last one hour of the simulation. The eight lines are representing different resolution results. Most of the figures are laid out with a dash line from MATLES code for comparison. The simulation results from D80 scheme and D80-R scheme are organized in top and bottom panel respectively. From left to right, three stability cases are laid out from surface cooling rate 0.25K/h to 1K/h with 0.5K/h in between. In addition, the time series in section 4.1.1 are plotted with same interval 5min as the data output descried in Section 3.2. Hereafter, the figures in statistical section (Sec. 4.1.1-4.1.3) have similar layouts as figure of mixing length and those descriptions shall not be duplicated.

Before diving into statistical description, the SGS mixing length as one key variable intersecting between the D80 and D80-R scheme is firstly presented in Fig. 4.1. From the top left panel of Figure 4.1, λ in the default cases equals to Δ in all grid spacing cases within a 100m region near the surface (Here after defined as Δ *zone*). Following Eq. 2.21, a range of grid spacing in this case are smaller than buoyancy length scale L_b as would be expected. The large value of L_b might be ascribed to either or both of the dominant value of SGS TKE (Fig. 4.15) and weakly stable stratification such that the stability criterion to use Lb is not satisfied (see Eq. 2.22). The similar explanation can be given to higher stability cases except that some differences are noticed for several grid spacing cases. The first difference is the height of Δ *zone*. The sinking of the height are from roughly 100m to 50m and 25m for surface cooling rate case of 0.25K/h to 0.50K/h and 1.00K/h respectively. From physical point of view, shallower boundary layer height caused by strong stability led to corresponding decreasing in each case. Based on Eq 2.23, the Brunt-Väisälä frequency turns larger as the stratification become stronger. As a result, the buoyancy length scale reduces to a large extent and the constrain of Δ becomes less strict (according to Eq. 2.21). The reduced restriction can be observed especially in very stable condition where the mixing length at coarser resolution cases is smaller than its grid size. In comparison to D80 scheme, the mixing length from D80-R (bottom panel of Fig. 4.1) almost increase linearly with height near the surface and reveals the dominant role of κz term (Eq. 2.32).

As the height goes to middle of stable boundary layer, the buoyancy length scale in D80-R takes over the role of mixing length and its dependence on grid spacing reveals remarkable in all three surface cooling rate cases. Clearly, coarser grid spacing contains more SGS TKE (Fig. 4.15) and thus leading to higher mixing length. In contrast, the values of mixing length stay with Δ for finer resolution in the

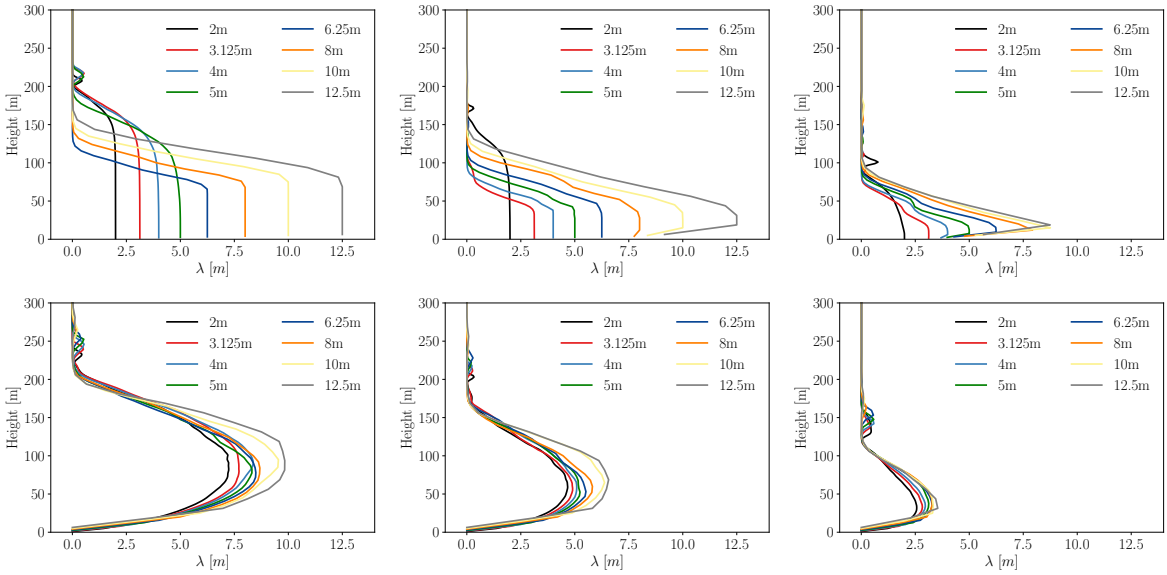

Figure 4.1: Vertical profile of the mixing length at last hour from D80 (top panel) and D80-R (bottom panel) in DALES and three cooling rate scenarios (0.25K/h: left panel; 0.50K/h: middle panel; 1.00K/h: right panel)

surface cooling rate of 0.25K/h because of the physical values of buoyancy length scale are still larger than Δ. With increasing stability, the occurrence of cases in finer resolution become less. In the case of 0.50K/h, only 2m shows the limitation of Δ. The decreasing occurrence in higher stability regime is ascribed to the reducing mixing length. The resolution which controls that limitation in each stability cases hereafter defined as *resolution threshold*.

In the upper part of boundary layer, both D80 and D80-R scheme shows monotonic decreasing trend of λ until its values reach zero in free atmosphere, which is due to the strong stratification. Additionally, the small jumps near the top of SBL happening in all D80-R case and several resolution cases in D80 runs are mainly due to the non-smooth transition from stable boundary layer to free atmosphere.

4.1.1. Time series

In this section, time series of surface friction velocity and sensible heat flux are documented in Fig. 4.2 and 4.3. First of all, the agreements between the modified Deardorff scheme of all resolution cases and dynamic code are remarkable both in surface friction velocity and surface sensible heat flux. However, the convergence become less satisfactory when it comes to more stable region especially for surface heat flux time series. In very stable cases of 1K/h cooling rate of the ground surface, the flux in momentum and heat field are slightly overestimated after two hours simulation time comparing to MATLES results. In the revised cases, the surface friction velocity time series reach quasi-equilibrium state after 5 h simulation time closing to 4 h documented in Beare et al. (2006). In contrast, the simulated surface sensible heat flux takes 7h to reach quasi-equilibrium state as reported in Huang and Bou-Zeid (2013).

In comparison, the default cases of the surface friction velocity and sensible heat flux present the similar *resolution threshold* effect in all stability cases. In 0.25K/h surface cooling rate case, the time series in friction velocity and sensible heat flux from grid size larger than 6.25m show laminar features over whole simulation time. As a comparison, de Roode et al. (2017) also observed the laminarized flow with intermittent resolved turbulence in the time series of resolved TKE. However, the lines of Δ finer than 6.25m fluctuate after 2 hours of turbulence “kick-off” time. The surface flux in coarser resolution could not surge into oscillated turbulence modeling after certain kick-off time (which may vary under different condition) on account of the *resolution threshold* effect. λ in coarser resolution is chosen to be Δ near the surface and this limits the development of turbulence. The new parameterization of mixing length (Eq. 2.32) takes presence of surface into account and wakes up the turbulence by reducing the mixing length near the surface. One reasonable evidence is that surface friction velocity and sensible heat flux in D80-R scheme start to fluctuate at the beginning of the simulation. In contrast, the finer resolution cases in D80 scheme with relatively smaller mixing length take around 2 hours and coarser

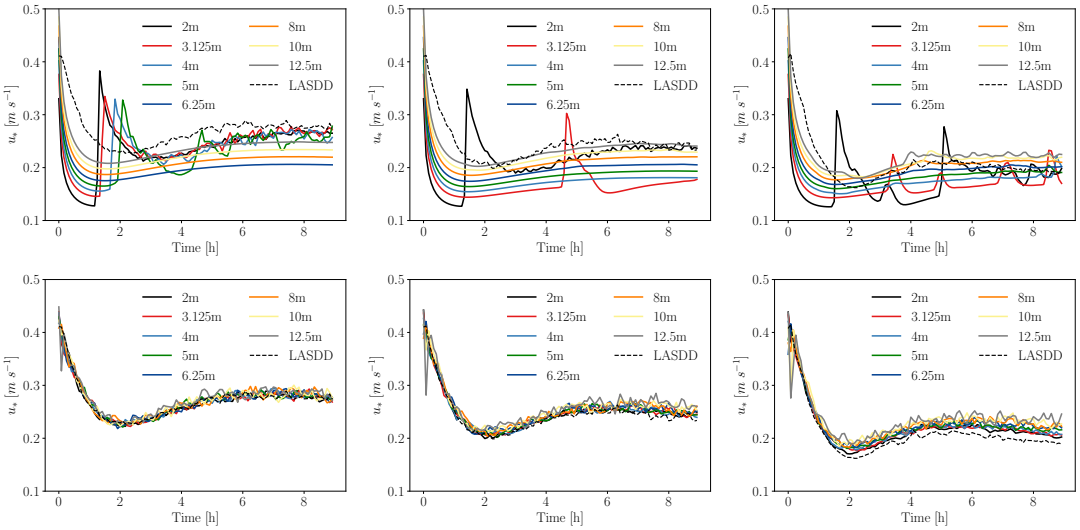

Figure 4.2: The time series of the surface friction velocity from D80 (top panel) and D80-R (bottom panel) in DALES and three cooling rate scenarios (0.25K/h: left panel; 0.50K/h: middle panel; 1.00K/h: right panel). The dashed black line represents the MATLES result

resolution cases never start turbulence. It is of importance to take presence of surface into account in the context of Deardroff SGS TKE scheme.

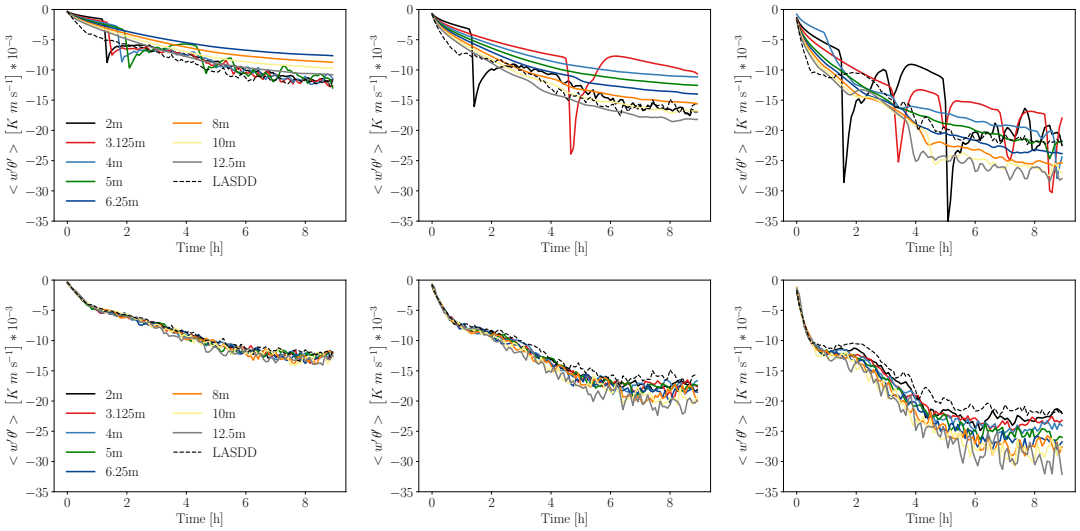

Figure 4.3: The time series of the surface sensible heat flux from D80 (top panel) and D80-R (bottom panel) in DALES and three cooling rate scenarios (0.25K/h: left panel; 0.50K/h: middle panel; 1.00K/h: right panel). The dashed black line represents the MATLES result (The legend in surface cooling rate of 0.50K/h and 1.00K/h are deactivated to avoid the overlap with profiles)

4.1.2. The first-order statistics

In Fig. 4.4, the vertical wind profiles from a range of resolution runs overlaid with dynamic code MATLES results are presented. It is remarkable that grid sensitivity of vertical wind profile in D80-R scheme diminished significantly by applying the new parameterization of mixing length. Taking surface cooling rate of 0.25K/h case as an example (bottom left panel of Fig. 4.4), the intensity of low-level jet (LLJ) and the height of maximum LLJ are captured strikingly well for all the resolution cases even 12.5m compared to the results from dynamic SGS code. As the surface cooling rate increases, the performance of the convergence become relatively poor than the case of 0.25K/h. Nevertheless, the spread of simulated wind profiles for all resolution cases are in reasonable range. In addition, the insignificant sensitivity in higher stability cases shows the dependence on grid size which shows the larger and lower LLJ from

finer resolution cases. Furthermore, the height of maximum LLJ become lower and magnitude of LLJ become stronger as the stability goes to higher regime. This conclusion is consistent with Huang and Bou-Zeid (2013).

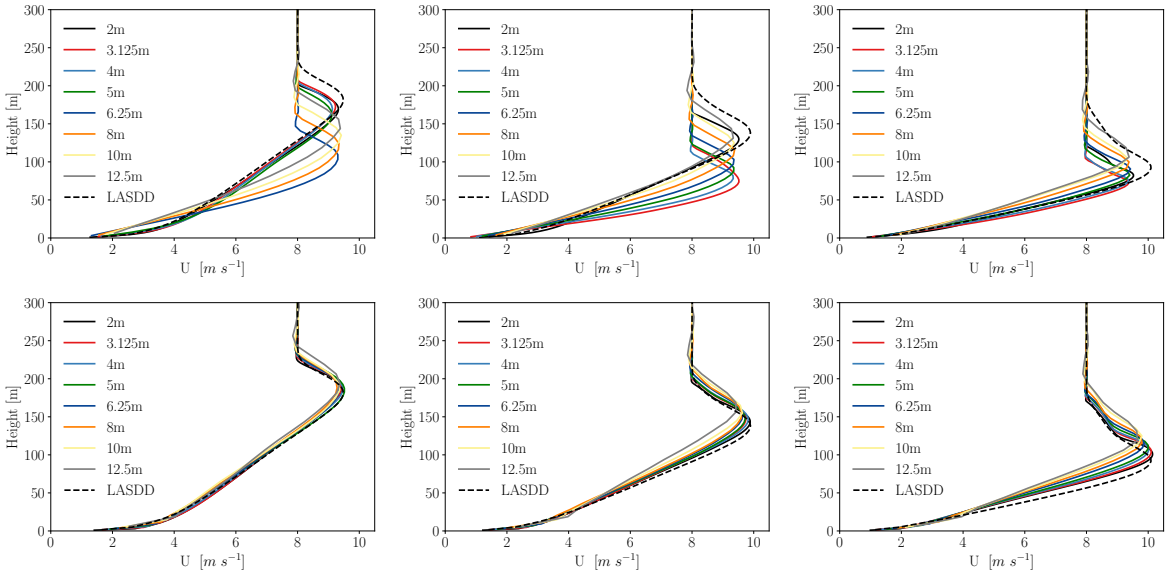

Figure 4.4: Vertical profile of mean wind speed at last hour from D80 (top panel) and D80-R (bottom panel) in DALES and three cooling rate scenarios (0.25K/h: left panel; 0.50K/h: middle panel; 1.00K/h: right panel). The dashed black line represents the MATLES result

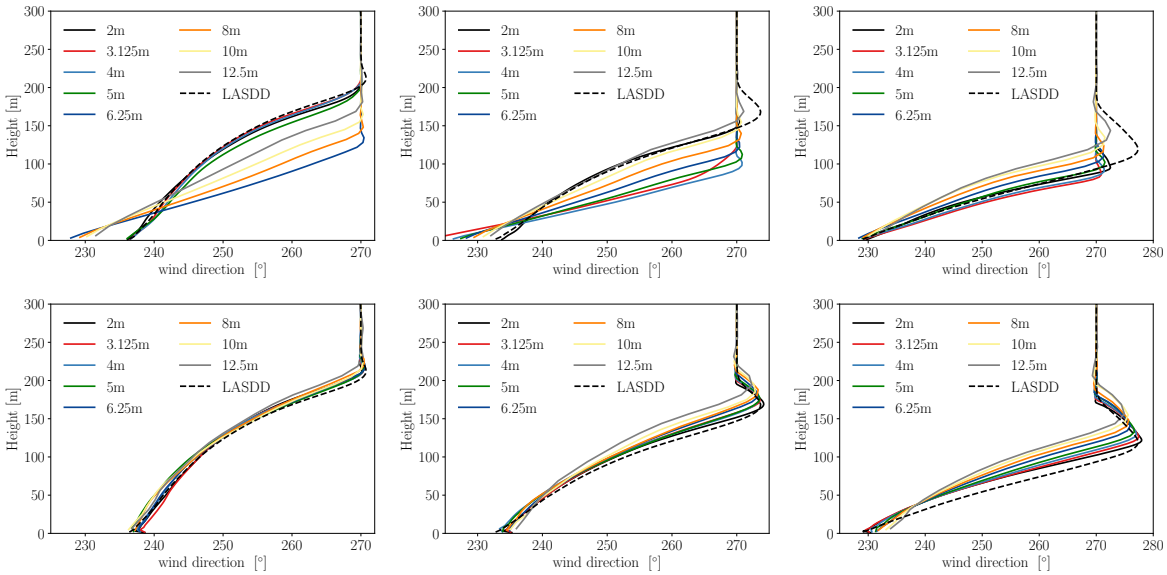

Figure 4.5: Vertical profile of wind direction at last hour from D80 (top panel) and D80-R (bottom panel) in DALES and three cooling rate scenarios (0.25K/h: left panel; 0.50K/h: middle panel; 1.00K/h: right panel). The dashed black line represents the MATLES result

Apart from D80-R cases, it is interesting to discuss the sensitivity behaviours showing in the D80 cases (top panel of Fig. 4.4). In all three cooling rate cases, the height of maximum LLJ shows strong sensitivity to resolution. However, it is noticeable this intensive sensitivity only takes effect for resolution coarser than 6.25m in case of surface cooling rate 0.25K/h, which corresponds to dissimilar behaviours of mixing length in the middle of SBL from D80 cases (top panel of Fig. 4.1). For the resolution finer than 6.25m, wind profile almost does not show sensitivity but the intensity of LLJ is underestimated.

One speculation of 6.25m as the grid size separating two dissimilar behaviour of mixing length and other variables lays in values of buoyancy length scale just above Δ zone. Around this region, L_b is in the range of 5m to 6.25m which leads to sharp decreasing of λ from coarser resolution cases and relatively unchanged λ from finer resolution. The Δ = 6.25m under 0.25K/h surface cooling rate case is defined before as the *resolution threshold*. The *resolution threshold* should shift to smaller grid size in higher stability regime due to stronger stratification. In the case of surface cooling rate 0.5K/h, the *resolution threshold* is 3.125m (Fig. 4.1 and 4.4). However, it is hard to observe the *resolution threshold* for 1K/h case because of very small mixing length in very stable condition.

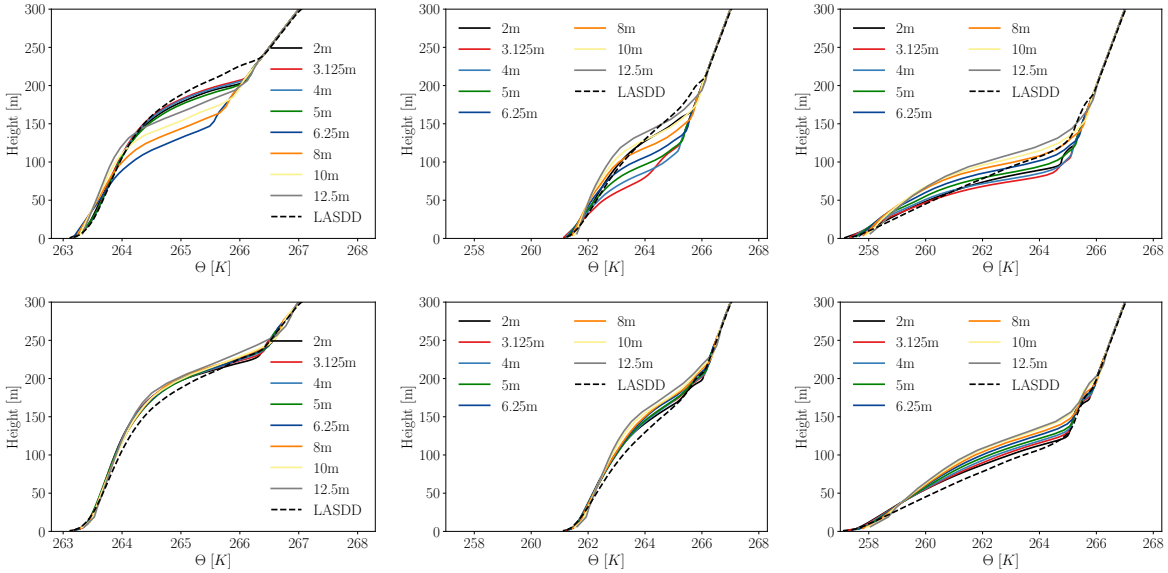

Figure 4.6: Vertical profile of potential temperature at last hour from D80 (top panel) and D80-R (bottom panel) in DALES and three cooling rate scenarios (0.25K/h: left panel; 0.50K/h: middle panel; 1.00K/h: right panel). The dashed black line represents the MATLES result. Please note the scale are inconsistent to show the shape of curvature in each case

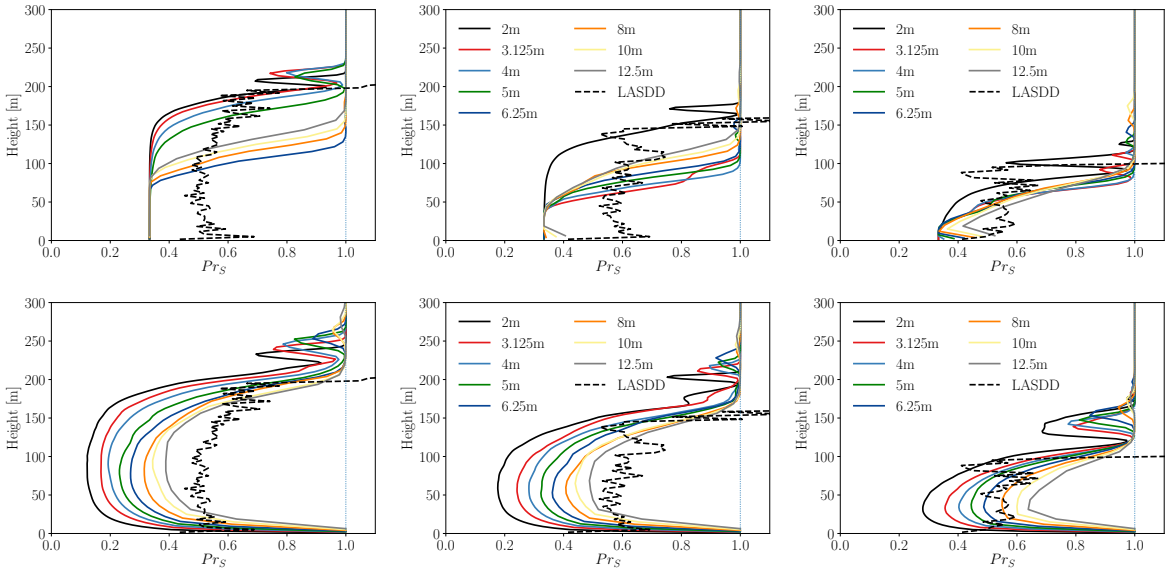

Figure 4.7: Vertical profile of Prandtl number at last hour from D80 (top panel) and D80-R (bottom panel) in DALES and three cooling rate scenarios (0.25K/h: left panel; 0.50K/h: middle panel; 1.00K/h: right panel). The dashed black line represents the MATLES result (The legend in surface cooling rate of 0.25K/h is deactivated to avoid the overlap with profiles)

In terms of wind turning angle presented in Fig. 4.5, the convergence of the simulated wind direction

from all resolution cases is remarkable and similar to the wind profile figures. In the study of Svensson and Holtslag (2009), the wind turning within boundary layer is linked to surface friction based on the analysis of GABLS1 intercomparison dataset. It is no wonder that both the wind direction profile and time series of surface friction velocity (Fig. 4.2) display unique convergence. Similar to wind profile, the sensitivity of the wind direction over height starts revealing as the surface cooling rate increases. Furthermore, the effects that shallower boundary layer and sharper wind turning above LLJ peak caused by higher surface cooling rate are also reported in Sullivan et al. (2016).

In the top panel of Fig. 4.5, the simulated wind direction by grid size coarser than their *resolution threshold* in each cooling rate cases are poorly captured by the default mixing length parameterization. Especially, the strong wind turning just above the LLJ peak is worse depicted by any resolution cases. In detail, the overestimation of the wind turning in the middle of SBL for surface cooling rate cases of 0.25K/h and 0.50K/h is due to the smaller surface friction (Fig. 4.2).

In terms of potential temperature presented in Fig. 4.6, the comparison of top panel and bottom panel once again proves that the implementation of new D80-R scheme diminishes the effects of *resolution threshold* shown in original D80 scheme. In the D80-R case of surface cooling rate 0.25K/h (bottom left panel in Fig. 4.6), the potential temperature profile displays the positive curvature near the top of SBL which is consistent with results in Beare et al. (2006). However, shape of curvature shows less positive features as the stability increases. Similarly, this vanished curvature reported in Sullivan et al. (2016) is exhibited. Furthermore, the discrepancy between the D80-R runs and dynamic runs in the middle of SBL is noticeable (0.25K/h: 150m-200m; 0.5K/h: 100m-150m; 1K/h: 50m-100m). The differences are ascribed to large heat diffusion because of the lower Prandlt number Pr_s shown in the bottom panel of Fig. 4.7. It is no wonder to see the large positive curvature in case of surface cooling rate 0.25K/h instead of 1.00K/h due to small Prandlt number. To further illustrate this in PALM model system (the setting of $c_m = c_h$), the potential temperature profile from D80-R scheme and dynamic code are perfectly identical (Fig. B.1 in Appendix B). In contrast. the underestimation of potential temperature caused by excessive heat diffusion is not visible in original D80 simulations in both model.

Fig. 4.7 shows the vertical distribution of SGS Prandtl number. In bottom panel, the values of Pr_s sharply dying from 1 as a result of linear increasing of κz term near the surface (based on Eq. 2.24 and Eq. 2.26). With nearly linear increase of λ, Pr_s decrease differently based on various resolution. In comparison, the mixing length from D80 runs equals to Δ in the Δ zone and thus leads to 0.33 of Pr_s value. As the height goes up, λ in D80-R depending on both κz and L_b may become large than grid size (refer to Fig. 4.1). Once again, based on Eq. 2.24 and Eq. 2.26, as a consequence, Pr_s in the case of larger mixing length reduce to the values lower than 0.33, which leads to strong heat diffusion. Moreover, the dependency between Pr_s and Δ in the middle of SBL is connected by dominant role of L_b. Near the top of SBL, the values of Pr_s in both D80 and D80-R scheme increase to unity as the mixing length reduces to zero (Fig. 2.21). Overall, the vertical distribution of Pr_s explains the underestimation and overestimation of temperature from D80-R and D80 respectively (Fig. 4.6).

4.1.3. The second-order statistics

In this section, the second-order statistics including vertical profile of momentum flux, sensible heat flux, variance and TKE are introduced and analyzed. The layout of the figures follows abovementioned prescription at the beginning of this chapter.

The total and resolved momentum flux (u and v component) displayed in figure 4.8, 4.9, 4.10 and 4.11. There are overall several observations can be made:

- The modification of new mixing length formulation in D80-R proves to have better performance in both total and resolved momentum flux (both u- and v-component). The simulated results agree well with MATLES simulations and the convergence of different resolution cases are clearly displayed. However, the spreads between resolutions become wider as the surface cooling rate increases. At the same time, the intensity of the momentum flux damped to weaker level due to strong stratification as documented in Huang and Bou-Zeid (2013). Additionally, it is notable that the sharp overestimation of the resolve momentum flux (both u- and v-component) in D80-R scheme are simulated especially in the cases of high stability regime. Nonetheless, one speculation is that the overpredicted intensity in very stable condition may due to unduly small mixing length, which leads to stagnation of energy in resolved scale. Because the smaller value of eddy viscosity and eddy diffusivity caused by smaller mixing length lead to less energy transferring from resolved scale to SGS scale.

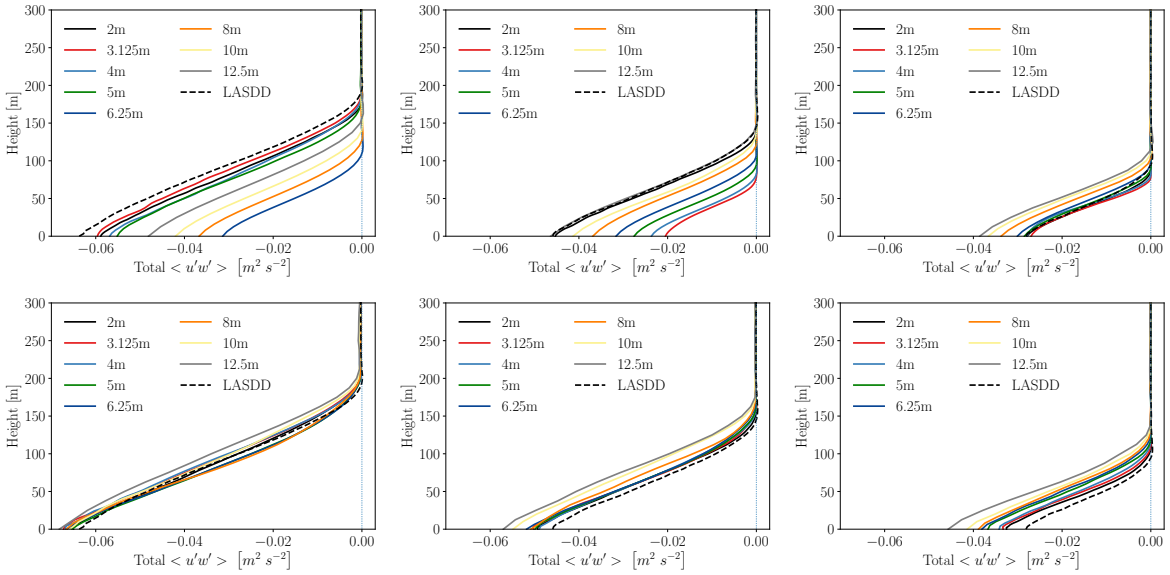

Figure 4.8: Vertical profile of total momentum flux (u-component) at last hour from D80 (top panel) and D80-R (bottom panel) in DALES and three cooling rate scenarios (0.25K/h: left panel; 0.50K/h: middle panel; 1.00K/h: right panel). The dashed black line represents the MATLES result

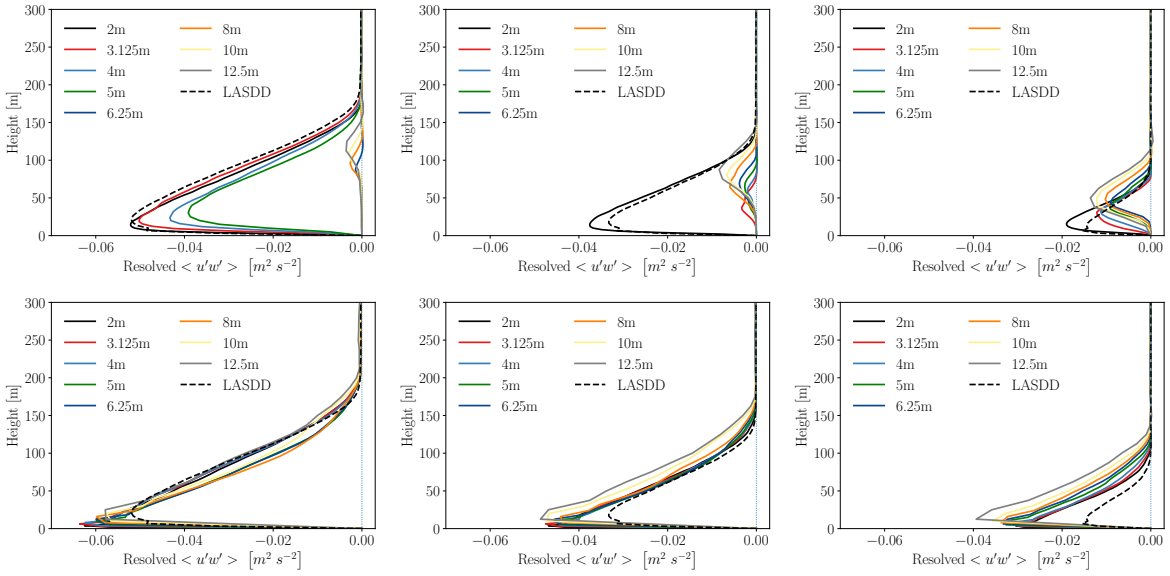

Figure 4.9: Vertical profile of resolved momentum flux (u-component) at last hour from D80 (top panel) and D80-R (bottom panel) in DALES and three cooling rate scenarios (0.25K/h: left panel; 0.50K/h: middle panel; 1.00K/h: right panel). The dashed black line represents the MATLES result

- In the original cases (top panel), the side effect of *resolution threshold* reveals especially in resolved momentum flux (both u- and v-component). It is apparent that $\Delta >$ *resolution threshold* cases barely resolve momentum flux within the stable boundary layer. In this circumstance, the major contribution to the total momentum flux is SGS momentum flux as a result of large grid spacing and unduly larger mixing length near the surface. In contrast to D80-R, the presence of surface wall introduced by κz term limits the intensity of visicosity near the surface and allows the momentum flux to be resolved in coarser resolution. Furthermore, in the case of 0.25K/h, the resolved momentum flux with dependence on grid spacing can be seen. Finer resolution have the ability to resolve more momentum flux (both u- and v-component) within the stable boundary layer. However, it is notable that the order of this dependence reverses as the stability increases

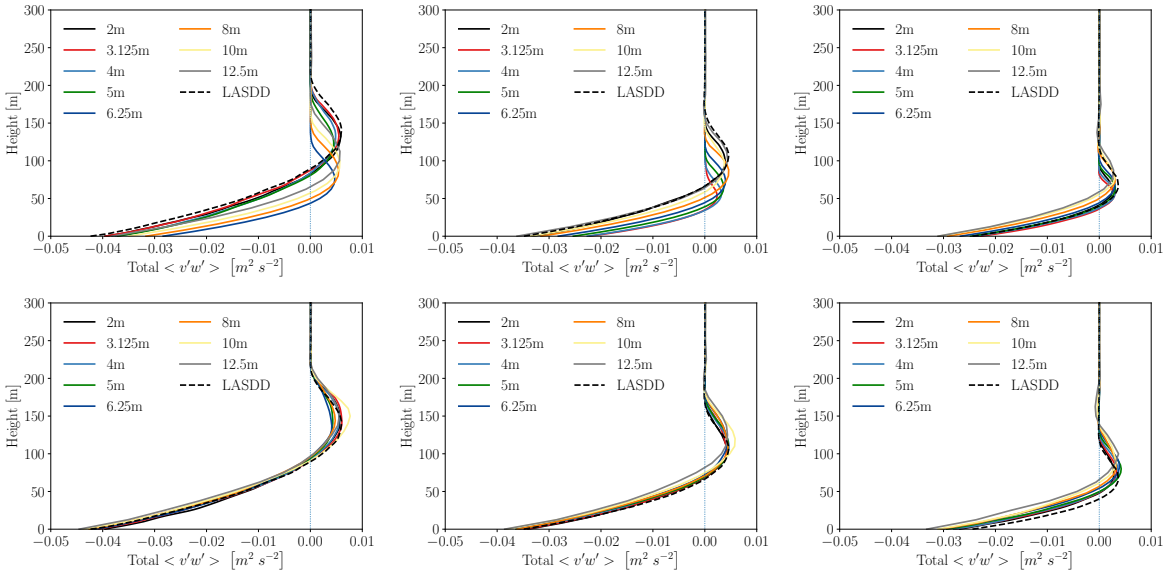

Figure 4.10: Vertical profile of total momentum flux (v-component) at last hour from D80 (top panel) and D80-R (bottom panel) in DALES and three cooling rate scenarios (0.25K/h: left panel; 0.50K/h: middle panel; 1.00K/h: right panel). The dashed black line represents the MATLES result

especially in resolved u-component momentum flux (bottom right panel of Fig. 4.9). In the case of 1K/h, coarser resolution runs display to have larger resolved momentum flux than finer resolution. Furthermore, the visibility of *resolution threshold* disappears because the insignificant mixing length in this very stable regime hardly limited by Δ. This similar trends can be depicted in total momentum flux.

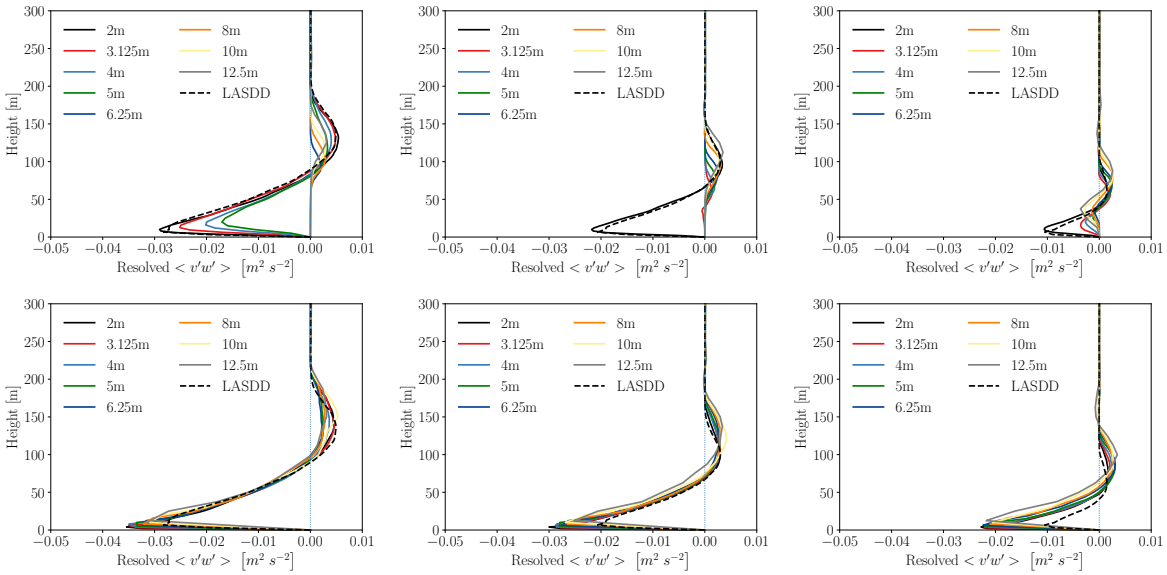

Figure 4.11: Vertical profile of resolved momentum flux (v-component) at last hour from D80 (top panel) and D80-R (bottom panel) in DALES and three cooling rate scenarios (0.25K/h: left panel; 0.50K/h: middle panel; 1.00K/h: right panel). The dashed black line represents the MATLES result

In Fig. 4.12 and 4.13, the total and resolved sensible heat flux are documented. The overall trend are similar to momentum flux profile. In the runs of D80-R (bottom panel), the agreement of simulated results between DALES and MATLES needs to be improved especially in the resolved sensible heat flux and higher stability regime. In the case of 0.25K/h (bottom left panel of Fig. 4.13), the overprediction

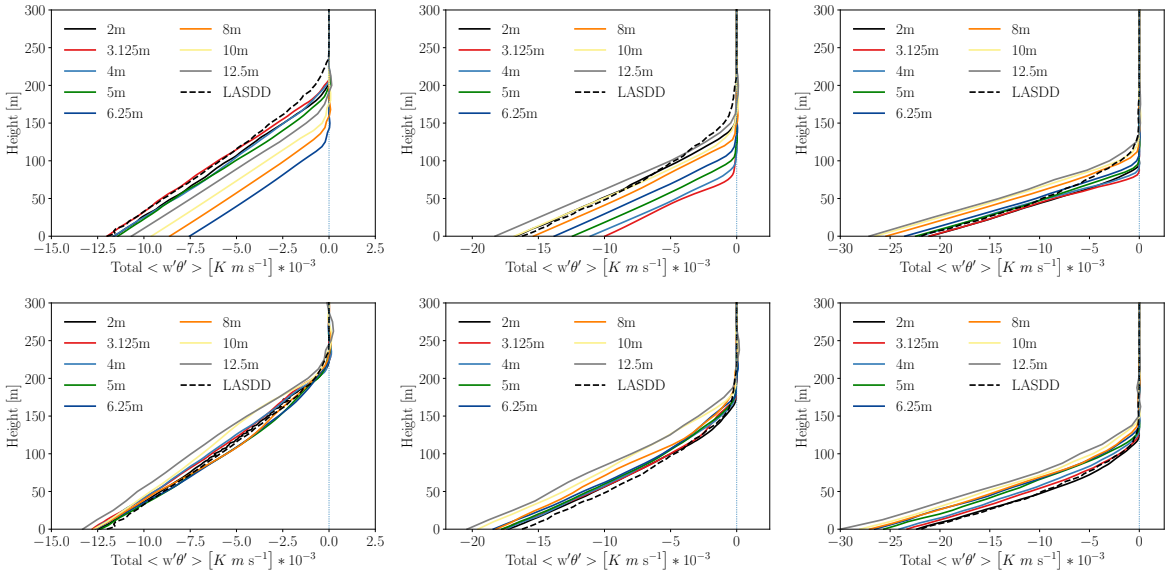

Figure 4.12: Vertical profile of total sensible heat flux at last hour from D80 (top panel) and D80-R (bottom panel) in DALES and three cooling rate scenarios (0.25K/h: left panel; 0.50K/h: middle panel; 1.00K/h: right panel). The dashed black line represents the MATLES result. The scale of all cooling rate cases are inconsistent for observation of trend of each case

near the surface and underestimation at upper height of the sensible heat flux are displayed. As the stability become stronger, the overestimation expands to whole stable boundary layer. Referring to vertical profile of Prandlt number (Fig. 4.7), the overestimation of sensible heat flux corresponds to the disproportionate unity of Prandlt number near the surface. The same evidence could be seen in higher stability regime.

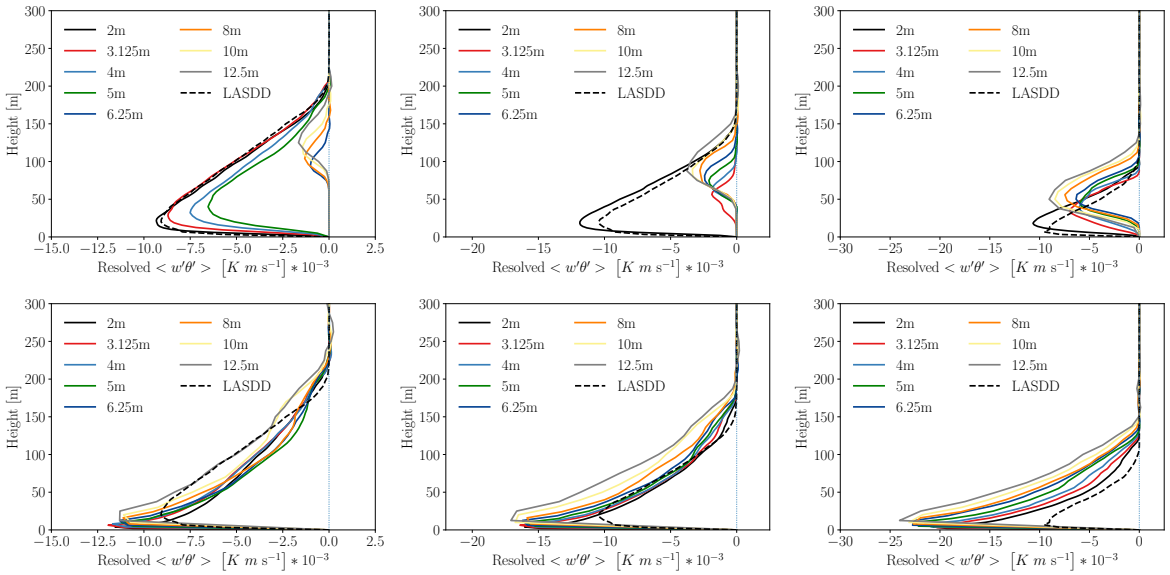

Figure 4.13: Vertical profile of resolved sensible heat flux at last hour from D80 (top panel) and D80-R (bottom panel) in DALES and three cooling rate scenarios (0.25K/h: left panel; 0.50K/h: middle panel; 1.00K/h: right panel). The dashed black line represents the MATLES result. The scale of all cooling rate cases are inconsistent for observation of trend of each case

In terms of original D80 scheme, identical effects of *resolution threshold* are presented. In the case of 1K/h (top right panel of Fig. 4.12 and 4.13), the performance of the simulation seems to beat other two stability cases in both total and resolved sensible heat flux. It is small buoyancy mixing length caused by strong stratification that avoids the problem of limitation of Δ and over-diffusion existing in

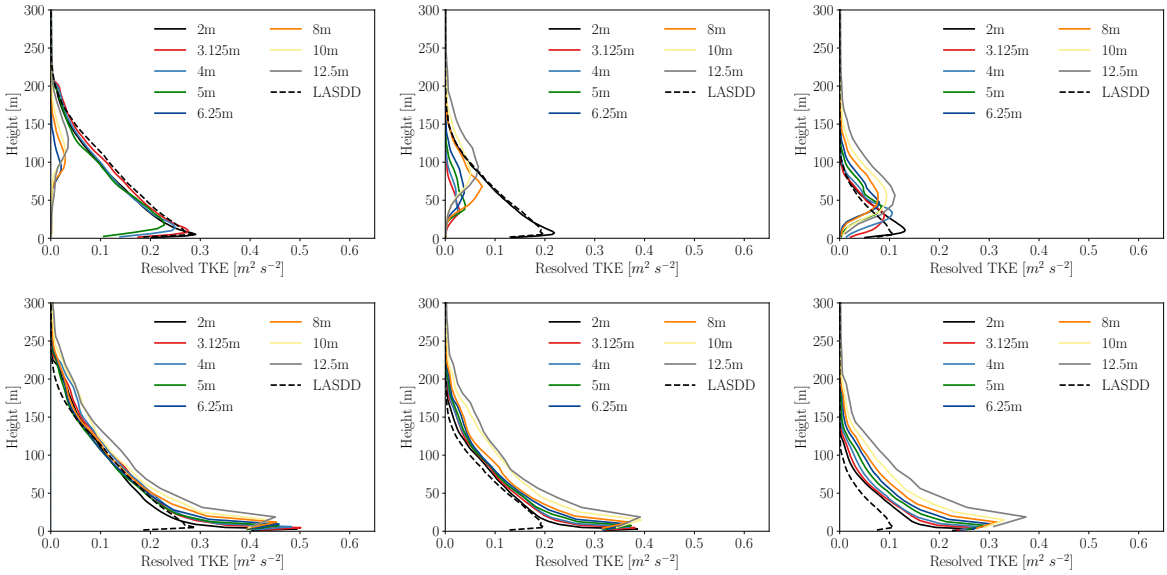

Figure 4.14: Vertical profile of resolved TKE at last hour from D80 (top panel) and D80-R (bottom panel) in DALES and three cooling rate scenarios (0.25K/h: left panel; 0.50K/h: middle panel; 1.00K/h: right panel). The dashed black line represents the MATLES result

D80-R case. The competition between the physical small buoyancy length scale and κz term due to presence of surface becomes intense in this circumstance. The issue puts a doubt on the application of κz term (Eq. 2.32) in the case of very stable boundary layer.

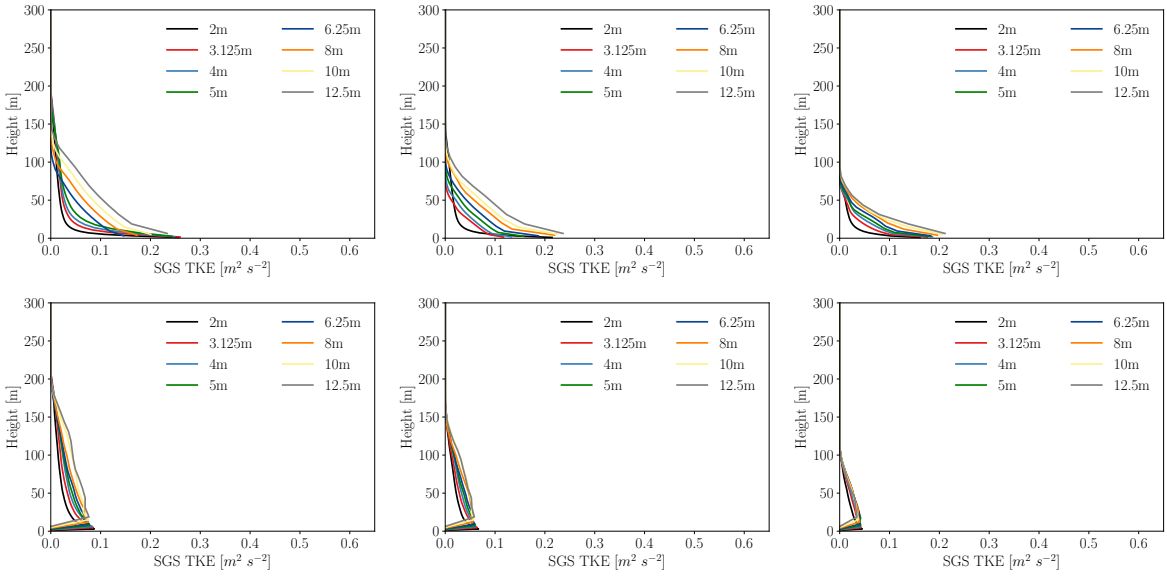

Figure 4.15: Vertical profile of SGS TKE at last hour from D80 (top panel) and D80-R (bottom panel) in DALES and three cooling rate scenarios (0.25K/h: left panel; 0.50K/h: middle panel; 1.00K/h: right panel). The dashed black line represents the MATLES result

The resolved and SGS TKE vertical profile are presented in Fig. 4.14 and 4.15. In Fig. 4.14, given abovementioned analysis, it is not surprising to observe the features of convergence of different resolution in D80-R scheme, *resolution threshold* effects in D80 scheme, decreasing resolved TKE and diminishing effects of *resolution threshold* with increasing stability. However, the overestimation of resolved TKE in D80-R cases is not in the same category as momentum and sensible heat flux. There are several speculations about this issue, one of which is addressed in additional analysis Sect. 4.3.

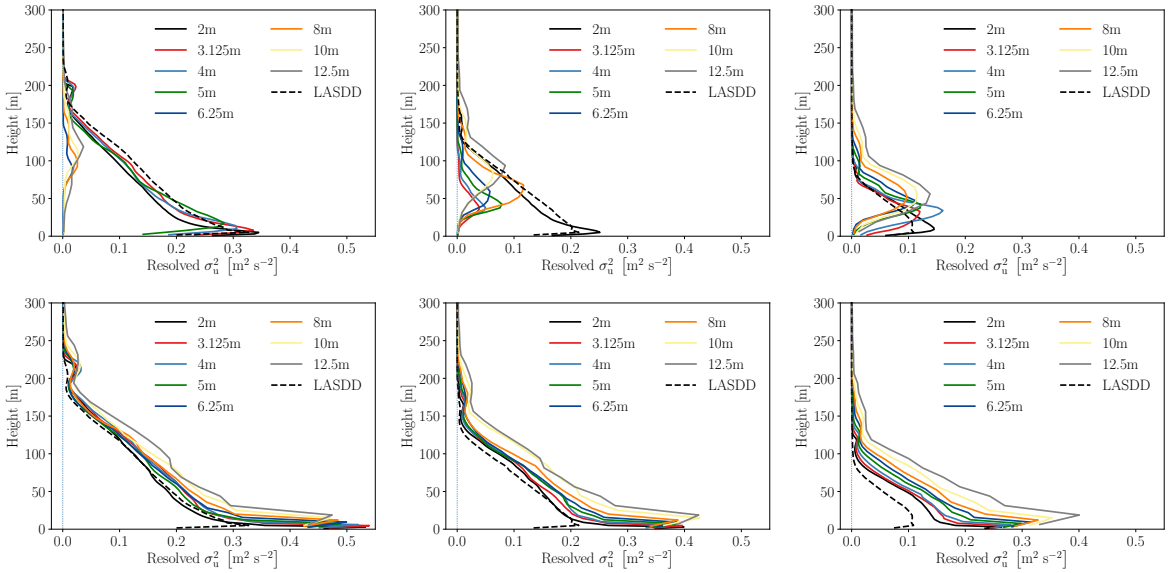

Figure 4.16: Vertical profile of resolved variance of the wind velocity(u component) at last hour from D80 (top panel) and D80-R (bottom panel) in DALES and three cooling rate scenarios (0.25K/h: left panel; 0.50K/h: middle panel; 1.00K/h: right panel). The dashed black line represents the MATLES result

The first one might be related to the dissipation rate near the surface. In Fig. 4.15, the small value of SGS TKE may lead to smaller dissipation rate with order of $3/2$ (Eq. 2.25) despite of small mixing length in the denominator. Another thinking concerns about simulated variance in Fig. 4.16, 4.17 and 4.18. The overprediction of resolved velocity variance in three dimension leads to large values of resolved TKE. The final speculation related to smaller value of mixing length in the context of Deardorff SGS TKE scheme. The resolved motions with less eddy viscosity contains more resolved energy when K_m decreases with unduly small λ. However, it is not clear which factor takes place in current study.

In terms of vertical profile of SGS TKE (Fig. 4.15), MATLES code system implements dynamic smagorinsky subgrid model and it does not solve the subgrid TKE equation. Thus there is no MATLES result overlaid. In the case of D80-R scheme, the contribution from SGS TKE comparing to resolved TKE are relatively small especially near the surface. The implementation of D80-R scheme in all resolution cases satisfies the requirement of successful LES simulation which should resolve 80% of total energy in the turbulent flow (Basu (2012)). Furthermore, the dependency on grid size could clearly be seen. Fine resolution cases contain less SGS TKE.

In Fig. 4.16, 4.17, 4.18 and 4.19, the vertical profile of the resolved variance of three dimensional velocity (σ_u^2, σ_v^2, σ_w^2) and potential temperature (σ_θ^2) are displayed. The resolved variance of velocity measures the intensity of turbulence fluctuations similar to the turbulence kinetic energy. Again, the similar feature of convergence and overestimation near the surface in D80-R, *resolution threshold* effect in D80 and decreasing intensity with increasing stability.

As for resolved variance of potential temperature, Fig. 4.19 reveals more features related to heat diffusion in three stability cases. In comparison to MATLES results, the convergence from D80-R scheme in 0.25K/h case is significant except around 200m height. The jumps of all the resolution cases around 200m might be caused by the sharp decrease of Pr_s number (Fig. 4.7). The transition from the top of the boundary layer to free atmosphere is not smooth and it leads to temperature fluctuation and larger variance of temperature. Below the transition area, the temperature variance is fully resolved. Regarding D80 scheme, the *resolution threshold* laminarized cases of coarser resolution within the Δ zone and the values of resolved σ_θ^2 get close to zero. The resolved variance shows in finer resolution corresponding to the resolved TKE (Fig. 4.14). The higher jumps from finer resolution similar to D80-R cases are again due to increasing trends of Pr_s at higher height.

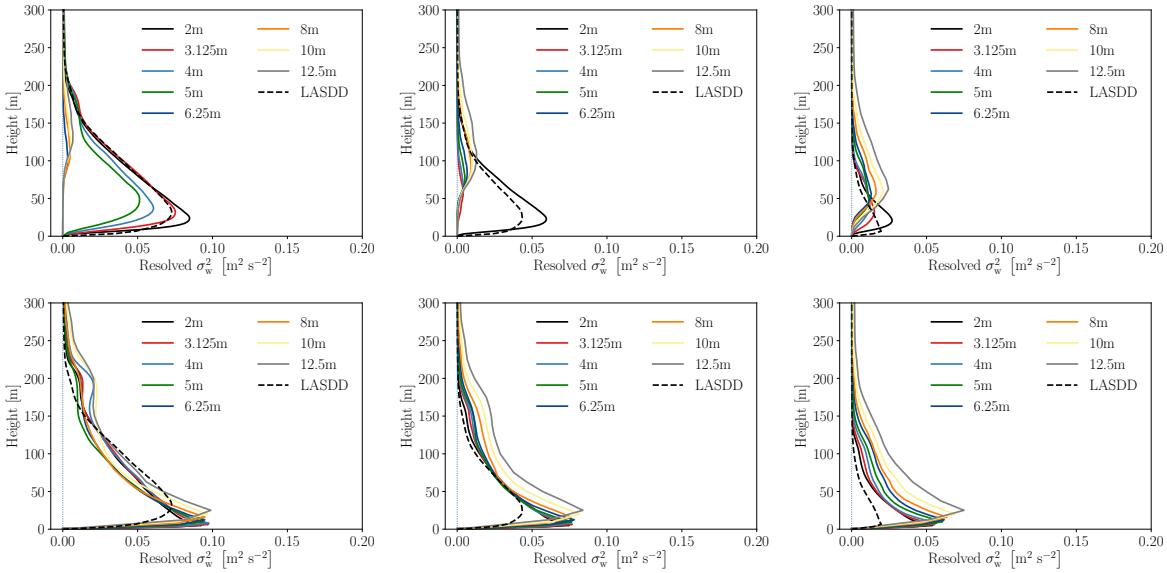

Figure 4.18: Vertical profile of resolved variance of the wind velocity(w component) at last hour from D80 (top panel) and D80-R (bottom panel) in DALES and three cooling rate scenarios (0.25K/h: left panel; 0.50K/h: middle panel; 1.00K/h: right panel). The dashed black line represents the MATLES result

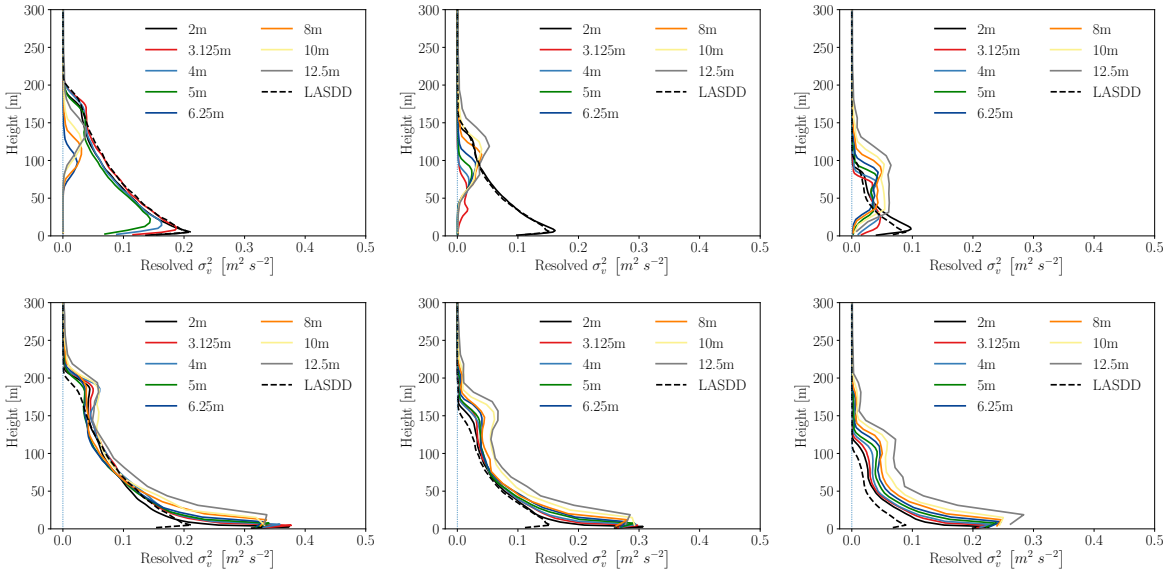

Figure 4.17: Vertical profile of resolved variance of the wind velocity(v component) at last hour from D80 (top panel) and D80-R (bottom panel) in DALES and three cooling rate scenarios (0.25K/h: left panel; 0.50K/h: middle panel; 1.00K/h: right panel). The dashed black line represents the MATLES result

When all stability cases are considered, the spreads of resolved variance from all the resolution cases are relatively wide. In the cases of D80 runs, the effect of *resolution threshold* again diminished at higher stability region due to smaller buoyancy length scale. The intensity of resolved variance goes to higher level due to the stronger stratification over the height in both D80 and D80-R scheme. It is interesting to notice that Δ = 2m case captures the resolve variance of potential temperature well in all the cases. This evidence proves that it is necessary to use finer resolution in very stable condition to resolve small turbulent structure.

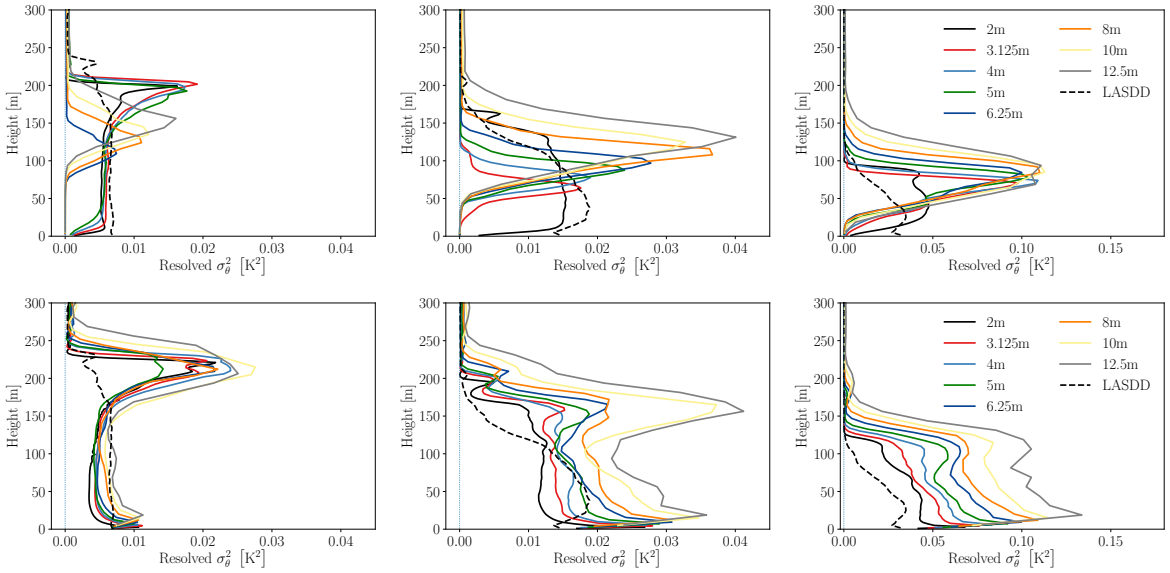

Figure 4.19: Vertical profile of resolved variance of potential temperature at last hour from D80 (top panel) and D80-R (bottom panel) in DALES and three cooling rate scenarios (0.25K/h: left panel; 0.50K/h: middle panel; 1.00K/h: right panel). The dashed black line represents the MATLES result. Please note the scales of all cases are inconsistent to show the trend in each case. Three cases share the same legend to avoid the overlap with profiles

4.2. The summary of statistics and discussion

In Sect. 4.1 of statistical analysis, the evaluation of the new implemented mixing length formulation is carried out based on comprehensive analysis of various variables, the comparison between original scheme and experiments of a range of stability regime. The overall improvement of the simulation results based on D80-R can be clearly observed in the accuracy of the intensity as well as convergence of a range of resolution runs. The progress of this new D80-R scheme can be noted down in perspective of how new included elements (Sect. 2.4.1) influence the simulation results. Although the dependence of resolution in the scheme of D80-R is related to the parameterization of c_h and c_ϵ. Despite of that, there are some discrepancy between DALES runs and MATLES in terms of TKE and variance near the surface.

- Based on the comparison between the D80 and D80-R runs, the fundamental limitations of D80 scheme are diagnosed in stable boundary layer. The *resolution threshold* near the surface is identified along with Δ zone because of the large buoyancy length scale. The constant Δ as mixing length within Δ zone on the one hand laminarized the turbulent flow, on the other hand unduly enlarge the eddy size near the surface. In detail, the large mixing length within Δ zone hampers the turbulence development from the surface.

- With the account of presence of surface using κz terms (Eq. 2.32), the *resolution threshold* identified in D80 scheme along with Δ zone disappear in the D80-R runs. The limitation of using finer resolution to simulate SBL is perfectly abolished as well. Thus, the surface time series, first order variables and second-order variables display remarkable convergence of the grid size in the stability close to moderately stable condition. The agreement between the converged results and MATLES results are striking.

- As the stability increase, the observation of lower boundary layer height, lower LLJ peak, higher intensity of LLJ, less positive curvature of potential temperature, smaller momentum flux and larger sensible heat flux can be noted (similar to Huang and Bou-Zeid (2013)). Furthermore, the mixing length turns smaller in this circumstance. The competition between κz and buoyancy length scale L_b encounters in lower height of SBL. The issue may lay in the central of physical mixing length parameterization.

- The excessive heat diffusion shown in the middle of SBL are ascribed to the values of Prandtl number smaller than 0.33. The prescribed formulation and parameters in original Deardorff SGS

TKE scheme may not be suitable for new proposed mixing length parameterization. Equation 2.24 and parameter c_m may need better improvement regarding the new mixing length formulation.

- In D80-R scheme, the disagreement of resolved TKE near the surface between DALES results and MATLES results can be observed. Although there is speculation that decreasing SGS TKE with $2/3$ order might lead to smaller dissipation rate, MATLES results may be slightly over dissipative near the surface.

4.3. Additional analyses

The new proposed mixing length parameterization are experimented in Sect. 4.1 and the overall performance is remarkable regarding the sensitivity of grid size and magnitude of physical variable. Section 4.2 summarizes the improvement of the statistics and the discrepancy between the dynamic SGS code and D80-R. In this section, additional analyses of D80-R in several aspects are carried out. The sensitivity of numerical model, the sensitivity of the advection schemes and prescribed parameter c_m is explored in Section 4.3.1. Some additional exploration regarding the point-wise conditional statement of stable boundary layer and second-order structure function near the surface are carried out.

4.3.1. The sensitivity analyses

In this section, The sensitivity experiments of D80-R are carried out in terms of numerical model, advection schemes built in DALES and the prescribed parameter c_m in Deardorff SGS TKE scheme.

The simulation results from PALM model

To test the independence of modification of mixing length parameterization on the LES code system, the simulation results of GABLS1 case from PALM model is included in appendix B. The setting differences between DALES and PALM are detailed in Sect. 3.2. Despite these differences, the improvement of convergence and quality of the simulation proves that the modification is independent of LES code system. Additionally, PALM code does not have the feature of excessive heat diffusivity in the middle of boundary layer shown in DALES results because of the setting of c_h equals to c_m. This further proves the deficiency of current parameterization of eddy diffusivity in D80-R.

Advection schemes

For advection scheme used in previous experiments, a 5th order advection scheme in horizontal direction and 2rd numerical scheme in vertical direction are implemented (called 52nd scheme). A variety of numerical schemes are built in DALES code system including second-order central difference scheme (2nd scheme), a fifth order scheme by adding a dissipative term to a sixth order scheme (5nd scheme), a hybrid scheme with a fifth order and WENO scheme (55nd scheme), a sixth order central difference scheme (6nd scheme), a sixth order scheme in horizontal and second-order in the vertical (62nd scheme) (Chiel van Heerwaarden (WUR)). The requirement of monotone numerical scheme need to adapt various scenarios. For example, 5nd scheme is a fifth order upwind scheme mainly account for small upwind gradient (Heus et al. (2010)). Although lower order scheme can handle the strong gradient of variables, it may suffer from the limitation of high numerical errors (Glendening and Haack (2001), Chow and Moin (2003)).

In this section, these numerical scheme are experimented using 6.25m resolution in DALES system. The simulation results are documented in Appendix C. It is striking that the D80-R scheme hardly display sensitivity to numerical scheme even with a second-order scheme. The evidence shown in this section proved that the observations observed in statistical section are mainly concerned to physical understanding of turbulent flow instead of numerical issues.

Parameter

In original and revised Deardorff SGS TKE scheme, the Deardorff parameter c_m is prescribed with a constant value 0.117 (approximated to 0.12 in Heus et al. (2010)). In DALES, this value is calculated using Eq. 4.1

$$c_m = \frac{c_\mathrm{f}}{2\pi}\left(\frac{3}{2}\alpha\right)^{-3/2} \tag{4.1}$$

where c_f=2.5 the filter constant and α is Kolmogorov constant 1.5. In this section, the Deardorff parameter c_m is modified to a set of values to test the sensitivity of D80-R to internal parameter by changing

the filter constant c_f. For experiments, the c_m equals to (0.071, 0.117, 0.165) when c_f is set to (1.5, 2.5, 3.5) respectively. The simulation results are included in Appendix D. The case of large c_m = 3.5 is out of trend from other two experiments because of high viscosity and diffusivity coefficient as a direct result of large c_m. The dominant contribution of SGS TKE and SGS flux explain how intensive the resolved motion transfer the energy to SGS scale. The limited development of turbulence in resolved level leads to shallower stable boundary layer. It is interesting to notice that the larger c_m cases have similar impacts to the cases of low resolution in D80. In the cases of D80, the mixing length from low resolution is force to be constant of large grid size near the surface. The counter-evidence further proves the limitation of using Δ with a min operator. Please note that the SGS TKE and SGS flux in case of c_m = 3.5 are dominant over the height comparing to other cases, which may not be real LES modelling (Basu (2012)). However it is for understanding the role of parameter in numerical scheme to represent stable boundary layer. In contrast, there is less sensitivity shown in smaller value of c_m because most of the turbulence structure are resolved in this case. This coincides with the mere sensitivity observed in fine resolution cases in D80 scheme.

4.3.2. Additional exploration

Conditional statement of stable boundary layer

In the context of Deardroff SGS TKE scheme, the conditional statement of defining stable boundary layer is based on instantaneous Brunt Vâisälä frequency N^2. The conditional code block is listed. When Brunt Vâisälä frequency N^2 is point-wise negative, the λ equals to Δ, otherwise, λ follows the original D80 (Eq. 2.21) or D80-R (Eq. 2.32).

```
if (ldelta .or. (dthvdz(i,j,k)<=0)) then
  zlt(i,j,k) = delta(k)
else
  zlt(i,j,k) =
      1/(1/(0.4*zh(k))+1/(cn*e120(i,j,k)/sqrt(grav/thvf(k)*abs(dthvdz(i,j,k)))))
```

Regarding the conditional statement of stable boundary layer using Brunt Vâisälä frequency N^2, there is an interesting debate between S.Lovejoy et al and Igor Esau. Lovejoy et al. (2008) questioned the notion of stable boundary layer by addressing the existence of Russian doll-like unstable layer within stable layer (called unstable sublayer in Lovejoy et al. (2008)). The drop sonde data with high resolution in both vertical and temporal scale are averaged into a range of layer thickness. Thinner layer with high resolution displays much more fractal hierarchy. To represent this variation even at low resolution, a power law scaling is proposed. However, Esau (2009) argued the misinterpretation of stable atmospheric layer concept from Lovejoy et al. (2008) is only based on instantaneous atmospheric stability and local turbulent variation. Furthermore, Esau (2009) stated the stability should be represented by coarser resolution such as the LESNIC numerical experiments. Later, Lovejoy et al. (2009) replied that the existence of instantaneous stability of the turbulent structure should be represented and not be suppress by artificially filterring. In this section, the statistics of Brunt Vâisälä frequency N^2 are analyzed in the context of D80 and D80-R scheme with three cooling rate cases.

Fig. 4.20 presents the vertical profile of averaged percentage of the positive Brunt Vâisälä frequency N^2 from D80 and D80-R scheme. In D80 scheme runs, the effects of *resolution threshold* as expected appear in moderately stable condition. Within the Δ zone, the laminarization of the flow caused by large constant Δ in low resolution cases leads to absence of unstable sublayer. In contrast, the Δ < *resolution threshold* follows the scaling theory discussed in Lovejoy et al. (2008). The conditional probability of embedded unstable sublayer originated from instantaneous stability and local turbulent structure depends on vertical resolution with inverse power law function. In comparison, this scaling theory applies to all resolution cases in D80-R scheme as well over the height except near the surface in all three cooling rate cases. The rapid increase of the condition probability of unstable sublayer might be ascribed to linear increase of κz term close to the wall. Moreover, a subtle trend of decreasing percentage can be seen as the stability becomes stronger. For one who attempts to parameterize this conditional probability in stable boundary layer, it is advised to incorporate stability term in formulation from Lovejoy et al. (2008).

The Structure function of velocity

Regarding the issue of dissipation rate near the surface in the vertical profile of resolved TKE, a second-order structure function of velocity is applied at 30m height. The calculation of structure function can

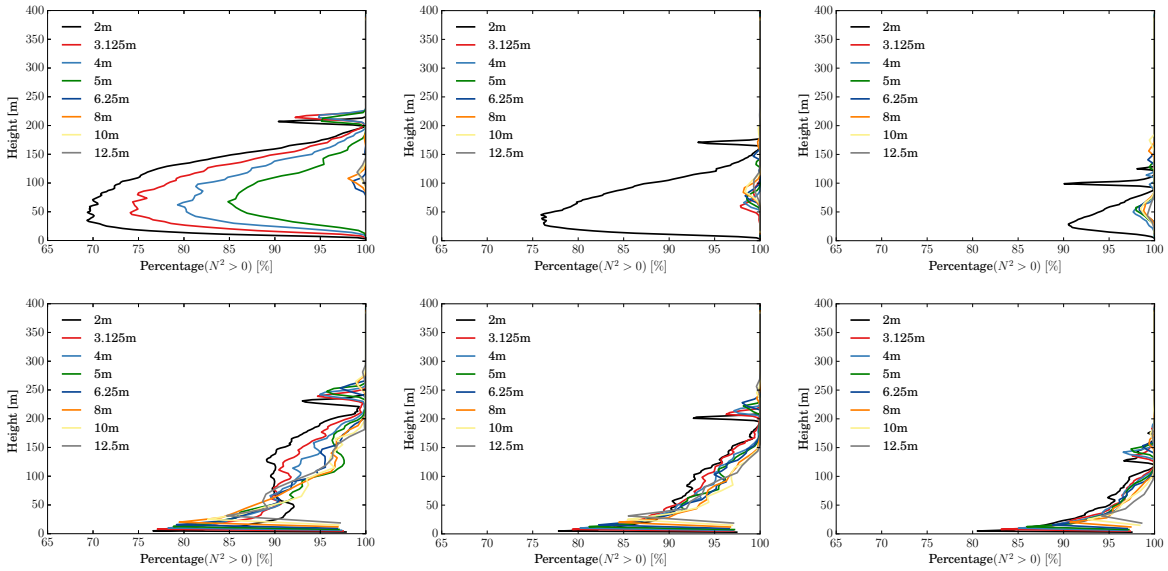

Figure 4.20: Vertical profile of percentage of the positive Brunt Vâisälä frequency N^2 at last hour from D80 (top panel) and D80-R (bottom panel) in DALES and three cooling rate scenarios (0.25K/h: left panel; 0.50K/h: middle panel; 1.00K/h: right panel)

be formulated in Eq. 4.2 following (Pope (2001)):

$$D_{nn}(r,x,t) \equiv \left\langle [U_i(x+r,t) - U_i(x,t)]^2 \right\rangle \tag{4.2}$$

Where the D_{nn} is second-order structure function, $U_i(x,t)$ and $U_i(x+r,t)$ are two point velocity at time t. It is found by Kolmogorov (1941a) that the second-order structure function increases with grid spacing (frequency) with order of $2/3$. (Pope (2001) and Van Atta and Chen (1970)). Furthermore, if Eq. 4.2 is expanded as following:

$$\begin{aligned} D_{nn}(r,x,t) &= \left\langle [U_i(x+r,t)]^2 \right\rangle + \left\langle [U_i(x,t)]^2 \right\rangle - 2\left\langle [U_i(x+r,t)U_i(x,t)]^2 \right\rangle \\ D_{nn}(r,x,t) &\approx \left\langle [U_i(x+r,t)]^2 \right\rangle + \left\langle [U_i(x,t)]^2 \right\rangle \\ D_{nn}(r,x,t) &\approx 2\sigma_u^2 \end{aligned}$$

The structure function could be approximated two time of velocity variance by neglecting the covariance between two distant points.

In Fig. 4.21, the left panel display the structure function at 30m height from various grid size cases in D80-R. It is noticeable that the trends from simulated result in DALES and MATLES code system are close to $2/3$ line. In high frequency region, all simulation results separate from theoretical line due to either numerical dissipation or physical dissipation. Except structure function from MATLES shows less dissipative feature than DALES results, the results from DALES follows the trend that coarser resolution cases dissipate more. The right panel shows structure function line from case of 4m resolution with the $2\sigma_u^2$ value overlaid, which proves the correction of derivation and validates the structure function. Due to the approximation in the derivation, the $2\sigma_u^2$ value is large than structure function line. Although MATLES result near the surface shows less dissipative features than DALES results, it is unknown that higher dissipation at 30m height in DALES code system is due to contribution of numerical or physical dissipation.

4.4. Summary and discussion

In this chapter, the evaluation of D80-R scheme are demonstrated by comparing with original scheme and testing under three cooling rate. The deficiencies of D80 and improvements of D80-R are summarized in Sect. 4.2. With further analyses of D80-R, several observation can be listed as following:

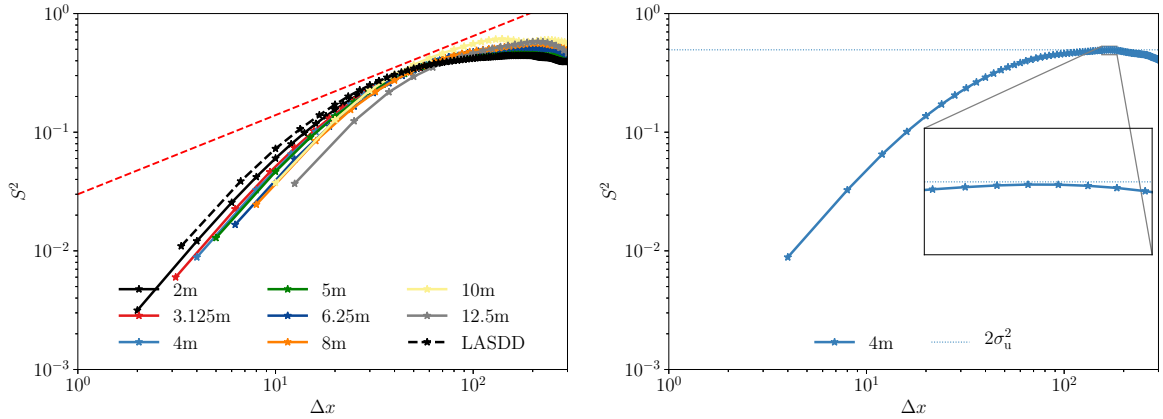

Figure 4.21: Left panel: The second-order structure function of velocity at 30 meter height. Different lines with star represent different resolution overlaid with dash-star line of MATLES results. The red dash line shows $2/3$ slope; Right panel: The structure function of 4m resolution and $2\sigma_u^2$ with blue-dot line at 30m height with a zooming window showing $2\sigma_u^2$ line is slight larger than 4m structure function line

- The D80-R scheme is independent of LES code system and shows little sensitivity to advection scheme. In terms of sensitivity of c_m, the results from case of larger c_m is out of trend of other cases because most of energy are transferring to SGS scale and the turbulence structure are not fully resolved. This feature is similar to the low resolution cases in D80 scheme.

- The numerical representation of unstable sublayer under stable condition has improved for all resolution cases with the implementation of new parameterization of mixing length. It is recommended to include grid size and stability both to parameterize the probability of the occurrence of unstable sublayer.

- Although the second-order structure function of velocity shows that MATLES results are less dissipative than results from DALES in high frequency region, it is still unknown that the overestimation of resolved TKE near the surface is due to numerical dissipation or numerical dissipation.

4.4.1. Discussion

In the study of Deardorff (1980), Deardorff brought up buoyancy length scale L_b to account for the smaller mixing length under stably stratified condition. It is assumed that buoyancy length scale should be smaller than grid size in the context of Deardorff SGS TKE scheme for many years. This leads to the question that is it legitimate to have the values of buoyancy length scale larger than grid size when the presence of surface is considered. On the one hand, the mixing length defined as the size of turbulent motions within SGS model, which means the mixing length should be smaller than filter width (Δ in context of DALES). However, the experiments of D80-R using a range of grid size under different stability condition justifies that the buoyancy length scale can predominantly exceed a normal grid size used under moderately stable condition near the surface. Moreover, the effects of wall on the development of turbulent motions should be interpreted. The presence of surface is considered in Deardorff (1980) by increasing the parameter of dissipation, however the κz term taken as mixing length near the surface exhibits potential capability.

This assumptions from original D80 scheme guarantee the values of SGS Prandtl varying between 0.33 for neutral or unstable condition and 1 for very stable condition. The violation of this assumption brings a problem of excessive heat diffusion in the middle of stable boundary layer because of oversize mixing length than grid size. This means the understanding of SGS Prandtl number and parameterization of c_h should be upgraded with the new proposed D80-R scheme. With the appreciation of previous parameterization in Deardorff (1980), the formulation in Gibbs and Fedorovich (2016) that considers that Prandtl number as a function of SGS TKE and gradient Richardson number may be a good starting point.

When the new proposed D80-R is considered in high stability region, the competition between κz and buoyancy length scale L_b become intense in a shallower boundary layer. The question comes to

the understanding and interpretation of interaction between the surface and turbulent flow in smaller scale. Thus, it is challenging to find and numerically define this critical point where the effect of one side take over another. The linear inverse operator might be limited under this complex condition. The higher order operator discussed in (Van de Wiel et al. (2008)) might have the possibility to handle this scenario.

5

Conclusion and future perspectives

In this study, several fundamental and inherent issues in the original Deardorfff SGS TKE scheme are identified under stably stratified condition. First of all, the *resolution threshold* caused by the encounter between the smaller grid size and large buoyancy length scale near the surface leads to misrepresentations of turbulent modelling. The constant Δ within Δ zone hampers the generation of turbulence in LES in two ways. The instantaneous dynamics are forced to diminish because of unchanged Δ and there is more energy transferring from resolved scale to SGS scale due to larger value of eddy viscosity and heat diffusivity as a result of large mixing length. The sensitivity of grid size caused by *resolution threshold* in coarser resolution is the result of the dominant role of SGS model in this circumstance. In contrast, although turbulent structure in finer resolution cases are mostly resolved due to small value of Δ to upper height. The constant Δ has the difficulty of portraying physical results.

The new proposed mixing length parameterization based on comprehensive experiments have shown promising simulated results not only in convergence of grid size but also in quality of the physical intensity. This new formulation has progressed in three ways. The substitution with Δ to κz delicately avoids the side effects of *resolution threshold* and takes the presence of surface into account. At the same time, the stability dependence is no longer limited by resolution. The inverse linear interpolation smooths the transition between the effects of wall and buoyancy. The small mixing length κz near the surface allows the turbulent development and initialization of LES modelling. In conclusion, this new D80-R scheme will have a beneficial effect on the simulations in stable boundary layer.

Despite of the remarkable performance of D80-R, several questions are brought up for further improvement of this scheme.

- The problem of excessive heat diffusivity related to low Prandlt number mainly concerns about the physical interpretation of connection between heat diffusivity and eddy viscosity. The parameterization of c_h shall be upgraded with the new implemented D80-R scheme.

- The overestimation of resolved TKE may be ascribed to under-dissipative feature of D80-R or over-dissipation of LASDD SGS model. However, it is difficult to distinguish the numerical dissipation and physical dissipation using spectrum analysis since DALES model is a finite-difference code. One possible way is to implement D80-R SGS scheme in a spectrum code (MATLES) for comparison.

- The modification from D80 scheme to D80-R scheme leads to indirect dependence of grid size. To enhance this dependence, one future direction will be to parameterize parameter c_m with the assumption of c_m is dependent of grid size. The simulation results may be improved.

- The understanding and interpretation of interaction between wall and turbulence under very stable condition requires further investigations. The complexity of turbulent motions may not be represented by simple inverse linear interpotation between the kz and buoyancy length scale. A higher order might be an option. Furthermore, is buoyancy length scale sufficient to account for the shear or stratification under stably stratified condition? The shear length scale discussed in Basu et al. (2020) may be an alternative to buoyancy length scale.

- The conditional probability of the unstable sublayer within the stable boundary layer in either numerical simulation or chaotic nature relates to the vertical resolution (Lovejoy et al. (2008)). Current study found that the parameterization of this quality should take stability into account.

A

DALES settings

This appendix contains setup processes of GABLS1 cases in DALES environment. To get familiar with DALES environment, a list of documents in `https://github.com/dalesteam/dales/tree/master/utils/doc/input` are taken as guidance and reference. It includes *dales-manual.pdf* detailed explaining starting up processes and model theory, *namoptions.pdf* which explains the meanings of all prescribed options.

The *namoption* file used in current study is shown (6.25m resolution case taken as an example). To apply this *namoption* file for all the resolution cases, the grid points ($itot, jtot, kmax$) in three dimension are certainly modified. Other options keep intact except $krand, ksp$ which controls the top level of randomnization and lower height of sponge layer respectively. Following the prescription in Beare et al. (2006), the gravity wave damping is applied above 300m and this height is not consistent with the calculation method used in DALES (Eq. A.1) when coarser resolution cases are implemented. The index level of randomnization related to initialization of LES model by adding perturbation near the surface.

$$k_sp = min(\frac{3}{4}K_{max}, k_{max} - 15) \tag{A.1}$$

The k_sp in cases of grid spacing Δ =12.5m, 10m and 8m is revised to 38, 31 and 24 respectively instead of calculation results 35, 25 and 17 using Eq. A.1. Similar to sponge layer, The top level ($krand$) of randomnization in resolution Δ = (12.5m, 10m, 8m, 6.25m, 5m, 4m, 3.125m, 2m) are set to (4, 5, 7, 8, 10, 13, 16, 25).

```
&RUN
iexpnr  = 000
runtime = 32400
dtmax   = 0.1
ladaptive = .false.
irandom = 43
randthl = 0.1
randqt  = 0.
randu   = 0.
krand   = 8
```

```
&DOMAIN
itot    = 64
jtot    = 64
kmax    = 64
xsize   = 400
ysize   = 400
xlat    = 73.
xlon    = 0.
ksp     = 48
```

```
&PHYSICS
ps       = 100000.00
thls     = 263.5
lcoriol  = .true.
iradiation = 0
z0       = 0.1
ltimedep = .true.
lmoist   = .false.
igrw_damp = 3
/
&NAMSURFACE
isurf    = 2
```

```
&NAMFIELDDUMP
lfielddump = .true.
dtav     = 300.
/
&NAMSUBGRID
ldelta   = .false.
/
&DYNAMICS
cu       = 7.
cv       = 0.
iadv_mom = 52
iadv_tke = 52
iadv_thl = 52
iadv_qt  = 52
```

The input files of GABLS1 experiment are created by GUN Data language (GDL referring to github page: `https://github.com/gnudatalanguage/gdl` and user guide: `https://personal.sron.nl/~kuiper/hea_inst11/exercise-2/GDL_IDL_doc/gdl.pdf`). There are many applications of GDL. In terms of creating data files with numbers and string, it often avoids garbled text format. The code used in current study is presented.

```
close,/all ;close any open file (if file is already open this will give an error)
ext     = 'G64' ;name of file extension
Nz = 64 ;number of vertical levels
Dz = 6.25 ;vertical grid resolution (m)

Nheader_lines = 2 ;header lines to explain meaning of variables in input files
prof_header = strarr(Nheader_lines)
prof_header(0) = 'gabls1 64'
prof_header(1) = ' height(m) thl(K) qt(kg/kg)  u(m/s)   v(m/s)   tke(m2/s2)'

lscale_header = strarr(Nheader_lines)
lscale_header(0) = 'gabls1 64'
lscale_header(1) = ' height(m) ugeo(m/s) vgeo(m/s) wfls(m/s) not_used not_used
    dqtdtls(kg/kg/s) dthldt(K/s) '

lsflux_header = strarr(Nheader_lines+1)
lsflux_header(0) = 'gabls1 64'
lsflux_header(1) = 'height ug vg wfls  not_used not_used dqtdt dthlrad '
lsflux_header(2) = '# 0.00000'

th_surf = 265. ;surface potential temperature
zero = 0.   ;variable to improve readability
deltath = 0.01 ;delta_th

;define prof.inp variables, initial state at t=0
zf = findgen(Nz) * dz + dz/2. ;height
thl = fltarr(Nz) ;liquid water potential temperature (K)
qt = fltarr(Nz) ;total water specific humidity (kg/kg)
u  = fltarr(Nz) ;wind velocity x-dir
v  = fltarr(Nz) ;         y-dir
tke = fltarr(Nz) ;initial turbulent kinetic energy at subgrid scales, needed for
    spin up

;lscale.inp
ugeo   = fltarr(Nz) ;geostrophic wind velocity x-dir
vgeo   = fltarr(Nz) ;                  y-dir
wfls  = fltarr(Nz) ;large-scale subsidence
dqtdtls = fltarr(Nz) ;large-scale tendency of qt
dthlrad = fltarr(Nz) ;large-scale tendency of thl, may include radiative tendency
```

```
;ls_flux.inp
gradthl = 1./100. ;thetal vertical gradient
Ug    = 8.     ;geostrophic wind in the x-direction
Vg    = 0.

dqtdx = zero
dqtdy = zero
dqtdt = zero

for k=0,Nz-1 do begin
   if zf(k) lt 100 then thl(k) = 265 else thl(k) = 265 + gradthl*(zf(k)-100)
   qt (k) = 0.
   u  (k) = Ug
   v  (k) = 0.
   if zf(k) lt 250 then tke(k) = 0.4*(1-zf(k)/250)*(1-zf(k)/250)*(1-zf(k)/250)
       else tke(k)=0
   Ugeo (k) = Ug
   Vgeo (k) = Vg
   wfls (k) = zero
   dqtdtls (k) = zero
   dthlrad (k) = zero
endfor

;write input data to files
prof_name = 'prof.inp.' + ext
lscale_name = 'lscale.inp.' + ext
lsflux_name = 'ls_flux.inp.' +ext

openw,1,prof_name
openw,2,lscale_name
openw,3,lsflux_name

for i=0,Nheader_lines-1 do printf,1,prof_header(i)
for k=0,Nz-1 do printf,1,format = ('(f10.5, f10.5,f10.6,f10.6,f10.6,f10.6)'),$
      zf(k),thl(k),qt(k),u(k),v(k),tke(k)

for i=0,Nheader_lines-1 do printf,2,lscale_header(i)
for k=0,Nz-1 do printf,2,format = ('(f10.6, 2f8.3, f10.6, 2f6.1, 2f6.1)'),$
      zf(k),Ugeo(k),Vgeo(k),wfls(k),dqtdx,dqtdy,dqtdtls(k),dthlrad(k)
for i=0,Nheader_lines do printf,3,lsflux_header(i)
for k=0,Nz-1 do printf,3,format = ('(f10.6, 2f8.3, f10.6, 2f6.1, 2f6.1)'),$
      zf(k),Ugeo(k),Vgeo(k),wfls(k),dqtdx,dqtdy,dqtdt,dthlrad(k)

close,1
close,2
close,3
END
```

During the experiments, one small bug identified in DALES version 4.2.1 is reported here for logging and reproducing of this study. The original subroutine around line 430 in file *modtimedep.f90* used to interpolate the prescribed surface condition over time is shown. The *rtimee* is the elapsed simulation time and the *timeflux(t)* is simulation time with larger interval corresponding to prescribed surface boundary condition. To interpolate the surface boundary condition at each time step, the condition in the code block find the right index to calculate the fraction at each elapsed time steps. However, the original subroutine predicts a wrong index at the end of simulation time by using *if (rtimee>timeflux(t)) then*. It should changed to *if (rtimee>timeflux(t-1)) then*.

```
   if(.not.(ltimedepsurf)) return
 !    --- interpolate! ----
   t=1
   do while(rtimee>timeflux(t))
```

```
  t=t+1
end do
if (rtimee>timeflux(t)) then
  t=t-1
endif
```

B

The simulation result from PALM model

The results from the PALM model system are documented in this appendix with the purpose to prove the model independence of the modification of mixing length parameterization. The similar trends are described in Sect. 4.1. For simplicity, the duplication of the description is avoid and only simulated results from D80-R scheme are shown.

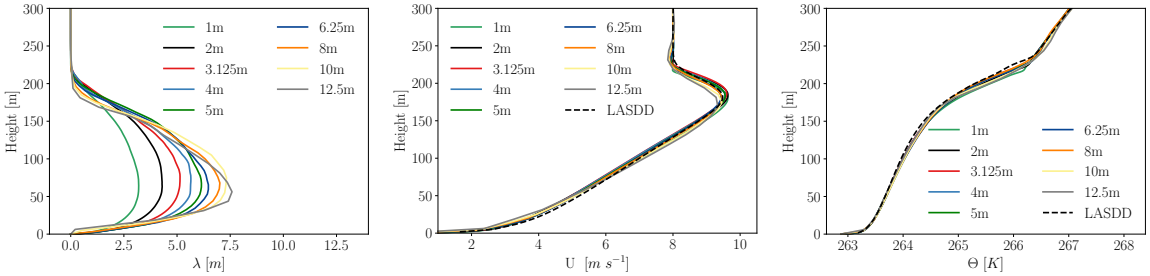

Figure B.1: Vertical profiles of mixing length (left panel), wind velocity (middle panel) and potential temperature (right panel) from D80-R scheme in PALM model system. Different colored lines correspond to different grid sizes (Δ). Results from the MATLES code are overlaid (dashed black lines) for comparison (except mixing length variable).

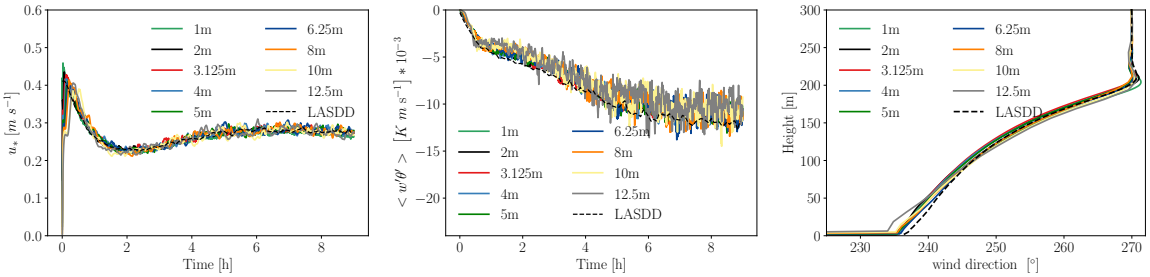

Figure B.2: Time series of surface friction velocity (left panel), sensible heat flux (middle panel) and vertical profile of wind direction (right panel) from D80-R scheme in PALM model system. Different colored lines correspond to different grid sizes (Δ). Results from the MATLES code are overlaid (dashed black lines) for comparison.

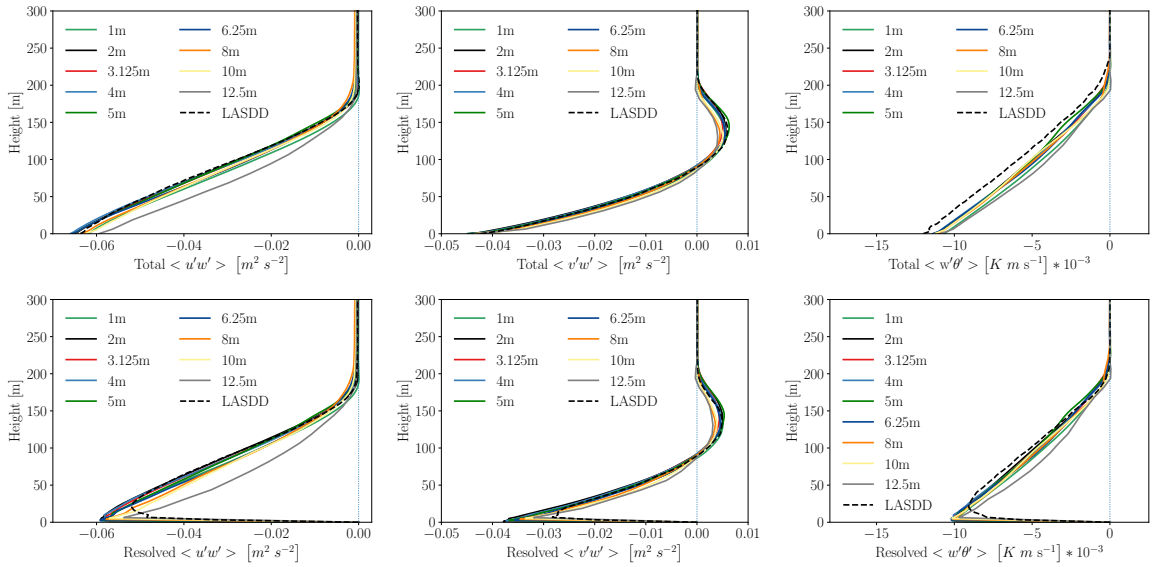

Figure B.3: Vertical profiles of total (top panel) and resolved (bottom panel) momentum flux (u-component left panel), (v-component middle panel) and sensible heat flux (right panel) from the D80-R scheme in PALM model system. Different colored lines correspond to different grid sizes (Δ). Results from the MATLES code are overlaid (dashed black lines) for comparison.

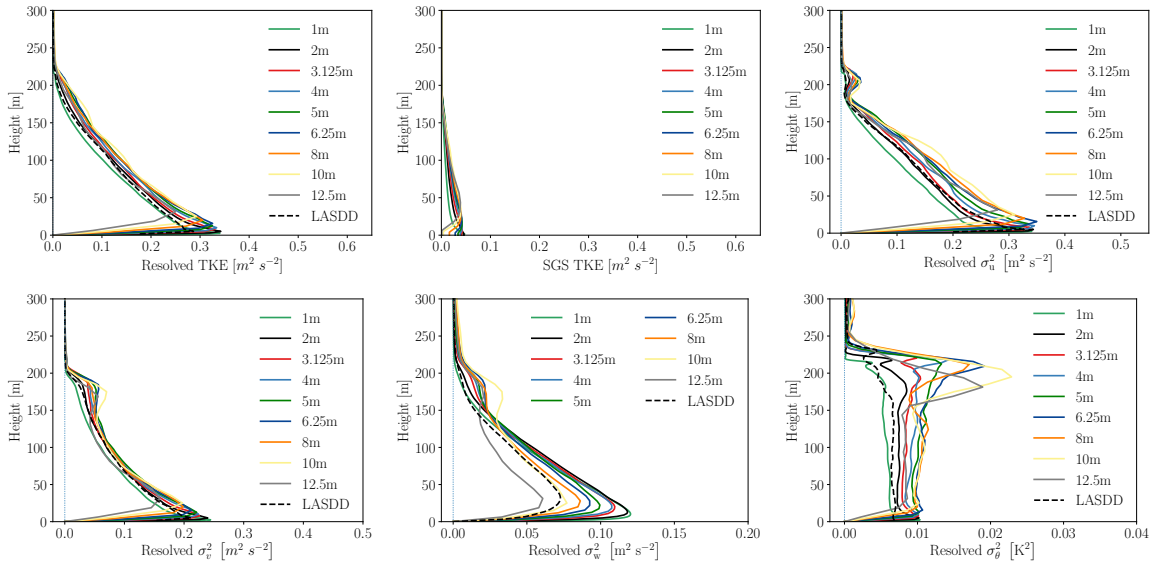

Figure B.4: Vertical profiles of resolved (top left panel) and subgrid-scale (top middle panel) turbulent kinetic energy, resolved variance of velocity (u-component top right panel), (v-component bottom left panel), (w-component bottom middle panel) and resolved variance of potential temperature (bottom right panel) from the D80-R scheme in PALM model system. Different colored lines correspond to different grid sizes (Δ). Results from the MATLES code are overlaid (dashed black lines) for comparison.

C

The sensitivity result of advection scheme

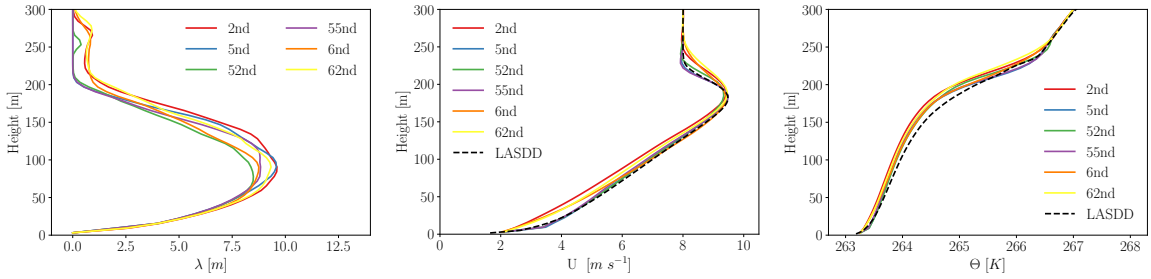

Figure C.1: Vertical profiles of mixing length (left panel), wind velocity (middle panel) and potential temperature (right panel) from D80-R scheme in DALES model system. Different colored lines correspond to different advection schemes. Results from the MATLES code are overlaid (dashed black lines) for comparison (except mixing length variable).

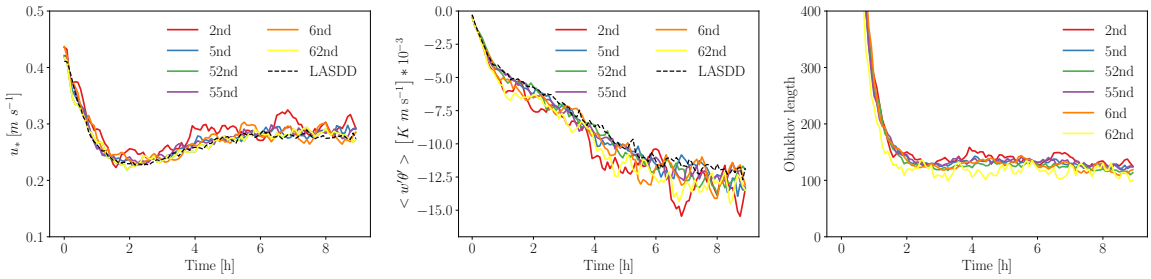

Figure C.2: Time series of surface friction velocity (left panel), sensible heat flux (middle panel) and Obukhov length (right panel) from D80-R scheme in DALES model system. Different colored lines correspond to different advection schemes. Results from the MATLES code are overlaid (dashed black lines) for comparison

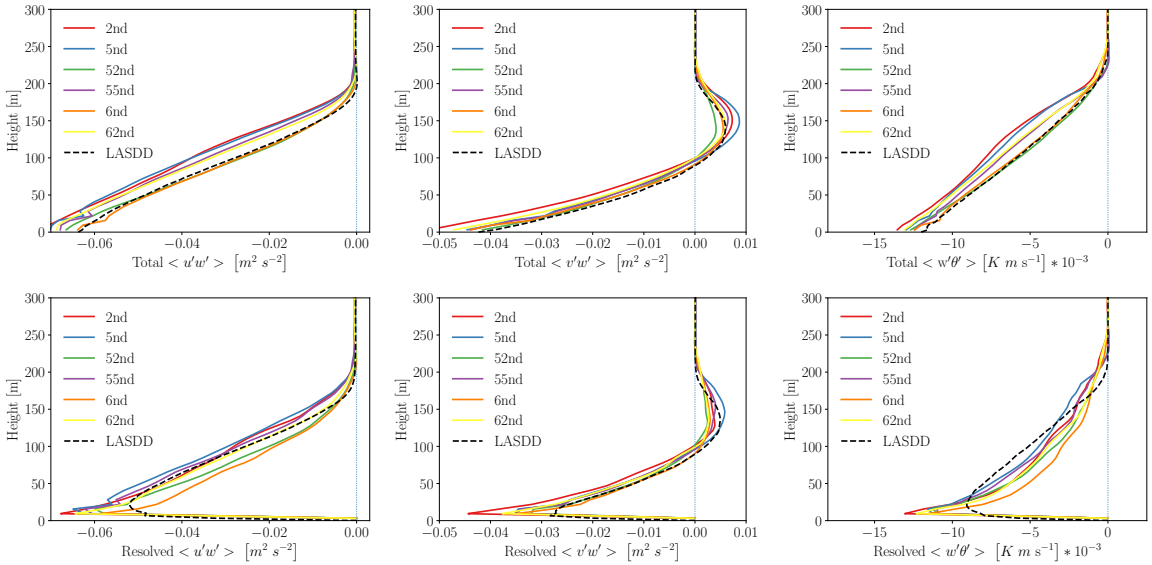

Figure C.3: Vertical profiles of total (top panel) and resolved (bottom panel) momentum flux (u-component left panel), (v-component middle panel) and sensible heat flux (right panel) from the D80-R scheme in DALES model system. Different colored lines correspond to different advection schemes. Results from the MATLES code are overlaid (dashed black lines) for comparison.

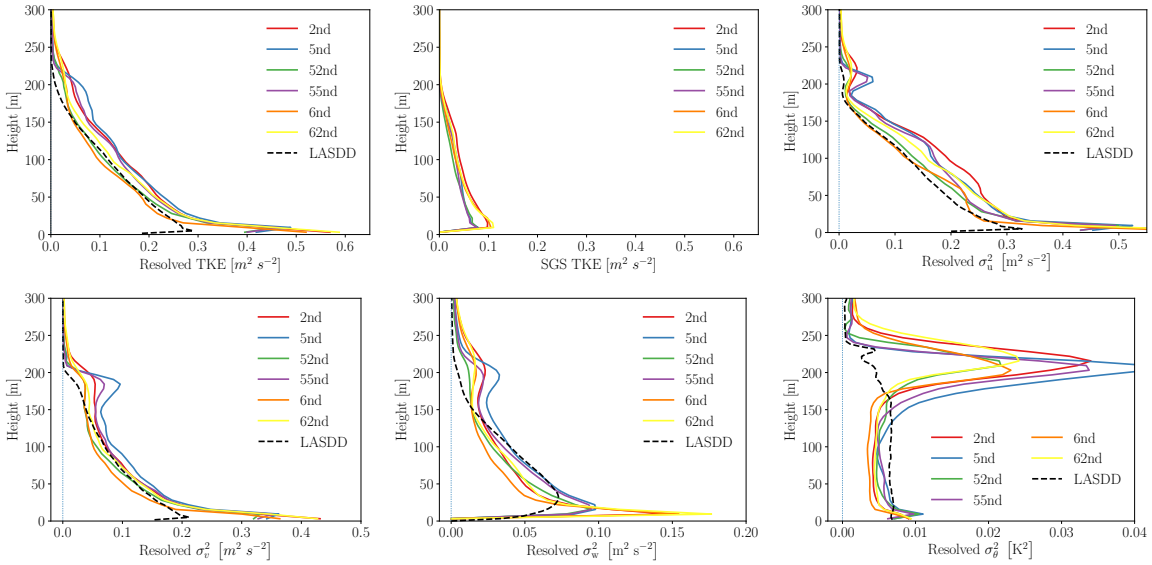

Figure C.4: Vertical profiles of resolved (top left panel) and subgrid-scale (top middle panel) turbulent kinetic energy, resolved variance of velocity (u-component top right panel), (v-component bottom left panel), (w-component bottom middle panel) and resolved variance of potential temperature (bottom right panel) from the D80-R scheme in DALES model system. Different colored lines correspond to different advection schemes. Results from the MATLES code are overlaid (dashed black lines) for comparison.

D

The sensitivity result of parameter c_m

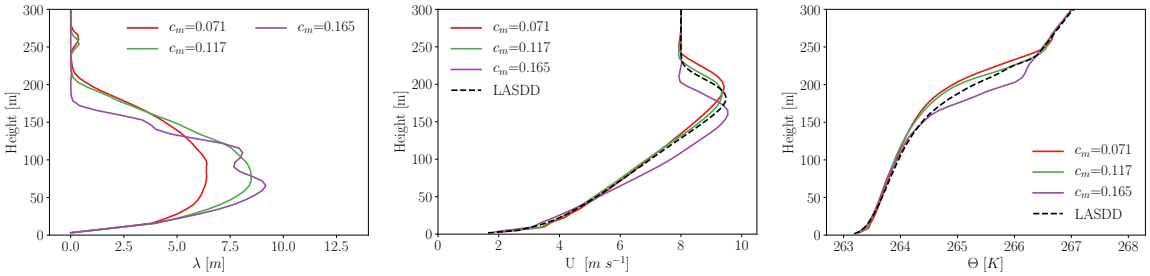

Figure D.1: Vertical profiles of mixing length (left panel), wind velocity (middle panel) and potential temperature (right panel) from D80-R scheme in DALES model system. Different colored lines correspond to different value of c_m. Results from the MATLES code are overlaid (dashed black lines) for comparison (except mixing length variable).

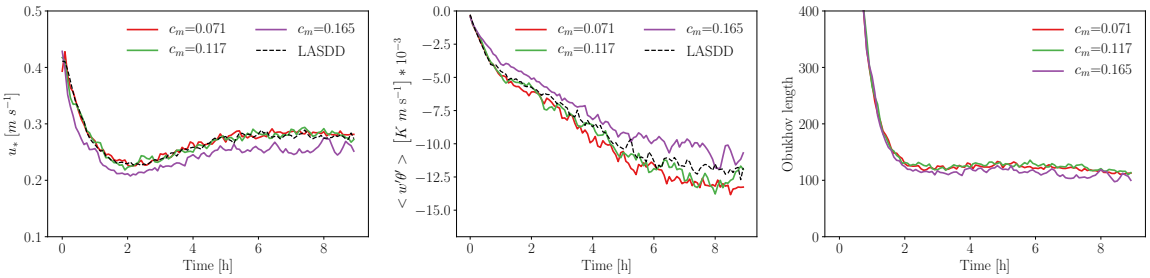

Figure D.2: Time series of surface friction velocity (left panel), sensible heat flux (middle panel) and Obukhov length (right panel) from D80-R scheme in DALES model system. Different colored lines correspond to different value of c_m. Results from the MATLES code are overlaid (dashed black lines) for comparison

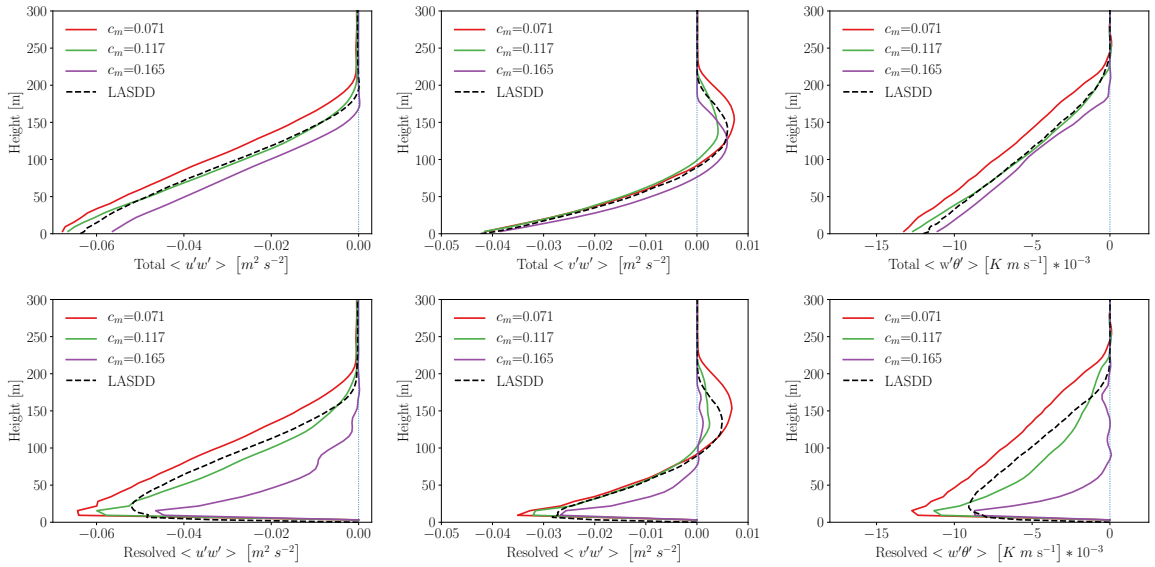

Figure D.3: Vertical profiles of total (top panel) and resolved (bottom panel) momentum flux (u-component left panel), (v-component middle panel) and sensible heat flux (right panel) from the D80-R scheme in DALES model system. Different colored lines correspond to different value of c_m. Results from the MATLES code are overlaid (dashed black lines) for comparison.

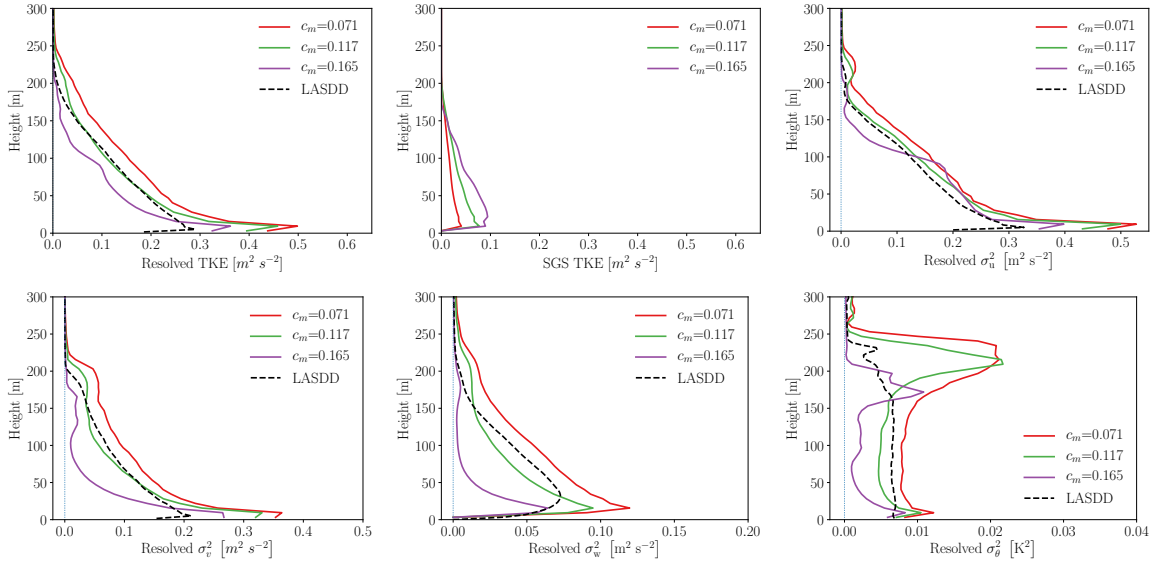

Figure D.4: Vertical profiles of resolved (top left panel) and subgrid-scale (top middle panel) turbulent kinetic energy, resolved variance of velocity (u-component top right panel), (v-component bottom left panel), (w-component bottom middle panel) and resolved variance of potential temperature (bottom right panel) from the D80-R scheme in DALES model system. Different colored lines correspond to different value of c_m. Results from the MATLES code are overlaid (dashed black lines) for comparison.

Bibliography

Abkar M, Moin P (2017) Large-eddy simulation of thermally stratified atmospheric boundary-layer flow using a minimum dissipation model. Boundary-layer meteorology 165(3):405–419

Andren A (1995) The structure of stably stratified atmospheric boundary layers: A large-eddy simulation study. Quarterly Journal of the Royal Meteorological Society 121(525):961–985

Baas P, de Roode SR, Lenderink G (2008) The scaling behaviour of a turbulent kinetic energy closure model for stably stratified conditions. Boundary-layer meteorology 127(1):17–36

Basu S (2012) Turbulent Flow Modeling, pp 273–281. DOI 10.1201/b13691-24

Basu S, Lacser A (2017) A cautionary note on the use of monin–obukhov similarity theory in very high-resolution large-eddy simulations. Boundary-Layer Meteorology 163(2):351–355

Basu S, Porté-Agel F (2006) Large-eddy simulation of stably stratified atmospheric boundary layer turbulence: a scale-dependent dynamic modeling approach. Journal of the Atmospheric Sciences 63(8):2074–2091

Basu S, Porté-Agel F, Foufoula-Georgiou E, Vinuesa JF, Pahlow M (2006) Revisiting the local scaling hypothesis in stably stratified atmospheric boundary-layer turbulence: an integration of field and laboratory measurements with large-eddy simulations. Boundary-Layer Meteorology 119(3):473–500

Basu S, Holtslag AA, Van De Wiel BJ, Moene AF, Steeneveld GJ (2008) An inconvenient "truth" about using sensible heat flux as a surface boundary condition in models under stably stratified regimes. Acta Geophysica 56(1):88–99

Basu S, Holtslag A, Bosveld F (2012) Gabls3-les intercomparison study. In: Proceedings of the Workshop on Diurnal cycles and the stable boundary layer, 7-10 November 2011, Reading, UK, pp 75–82

Basu S, He P, DeMarco AW (2020) Parameterizing the energy dissipation rate in stably stratified flows. Under Review, available at: https://arxiv.org/abs/2001.02255

Beare RJ, Macvean MK, Holtslag AAM, Cuxart J, Essau I, Golaz JC, Jimenez MA, Khairoutdinov M, Kosovic B, Lewellen D, Lund TS, Lundquist JK, Mccabe A, Moene AF, Noh Y, Raasch S, Sullivan P (2006) An intercomparison of large-eddy simulations of the stable boundary layer. Boundary-Layer Meteorol 118:247–272

Berselli L, Iliescu T, Layton W (2006) Mathematics of large eddy simulation of turbulent flows. Springer

Bhaganagar K, Debnath M (2015) The effects of mean atmospheric forcings of the stable atmospheric boundary layer on wind turbine wake. Journal of Renewable and Sustainable Energy 7(1):013,124

Blackadar AK (1962) The vertical distribution of wind and turbulent exchange in a neutral atmosphere. Journal of Geophysical Research 67(8):3095–3102

Bradshaw P (1974) Possible origin of prandt's mixing-length theory. Nature 249(5453):135–136

Brost R, Wyngaard J (1978) A model study of the stably stratified planetary boundary layer. Journal of the Atmospheric Sciences 35(8):1427–1440

Brown AR, Derbyshire S, Mason PJ (1994) Large-eddy simulation of stable atmospheric boundary layers with a revised stochastic subgrid model. Quarterly Journal of the Royal Meteorological Society 120(520):1485–1512

Buzzi M, Rotach MW, Holtslag M, Holtslag AA (2011) Evaluation of the cosmo-sc turbulence scheme in a shear-driven stable boundary layer. Meteorologische Zeitschrift 20(3):335–350

Chow FK, Moin P (2003) A further study of numerical errors in large-eddy simulations. Journal of Computational Physics 184(2):366–380

Cuxart J, Holtslag AA, Beare RJ, Bazile E, Beljaars A, Cheng A, Conangla L, Ek M, Freedman F, Hamdi R, et al. (2006) Single-column model intercomparison for a stably stratified atmospheric boundary layer. Boundary-Layer Meteorology 118(2):273–303

Davidson PA, Kaneda Y, Moffatt K, Sreenivasan KR (2011) A voyage through turbulence. Cambridge University Press

Deardorff JW (1980) Stratocumulus-capped mixed layers derived from a three-dimensional model. Boundary-Layer Meteorol 18:495–527

Degrazia GA, Moraes OL, Oliveira AP (1996) An analytical method to evaluate mixing length scales for the planetary boundary layer. Journal of Applied Meteorology 35(6):974–977

Donda J, Van de Wiel B, Bosveld F, Beyrich F, van Heijst G, Clercx H (2013) Predicting nocturnal wind and temperature profiles based on external forcing parameters. Boundary-layer meteorology 146(1):103–117

van Dop H, Axelsen S (2007) Large eddy simulation of the stable boundary-layer: A retrospect to nieuwstadt's early work. Flow, turbulence and combustion 79(3):235–249

Ďurán IB, Geleyn JF, Váňa F, Schmidli J, Brožková R (2018) A turbulence scheme with two prognostic turbulence energies. Journal of the Atmospheric Sciences 75(10):3381–3402

Enriquez RM, Street RL (2014) Large-eddy simulation of the stable boundary layer: revisiting gabls with a linear algebraic subgrid-scale turbulence model. In: 21st symposium on boundary layers and turbulence, American Meteorological Society B, vol 14

Esau I (2009) Comment on" do stable atmospheric layers exist?" by s. lovejoy et al. Geophysical research letters 36(11)

Galmarini S (1998) Stable nocturnal boundary layers: a comparison of one-dimensional and large-eddy simulation models. Boundary-layer meteorology 88(2):181–210

Germano M, Piomelli U, Moin P, Cabot WH (1991) A dynamic subgrid-scale eddy viscosity model. Physics of Fluids A: Fluid Dynamics 3(7):1760–1765

Geurts BJ (2003) Elements of direct and large eddy simulation. RT Edwards, Inc

Geurts BJ, Fröhlich J (2002) A framework for predicting accuracy limitations in large-eddy simulation. Physics of fluids 14(6):L41–L44

Gibbs JA, Fedorovich E (2016) Sensitivity of turbulence statistics in the lower portion of a numerically simulated stable boundary layer to parameters of the Deardorff subgrid turbulence model. Q J R Meteorol Soc 142:2205–2213

Glendening JW, Haack T (2001) Influence of advection differencing error upon large-eddy simulation accuracy. Boundary-layer meteorology 98(1):127–153

van Heerwaarden C, Van Stratum BJ, Heus T, Gibbs JA, Fedorovich E, Mellado JP (2017) Microhh 1.0: a computational fluid dynamics code for direct numerical simulation and large-eddy simulation of atmospheric boundary layer flows. Geoscientific Model Development 10:3145–3165

Chiel van Heerwaarden (WUR) SdRTD Thijs Heus (KNMI) (2009) Dales guidance. `https://github.com/dalesteam/dales/tree/master/utils/doc/input`

Heus T, van Heerwaarden CC, Jonker HJJ, Siebesma AP, Axelsen S, van den Dries K, Geoffroy O, Moene AF, Pino D, de Roode SR, Vilà-Guerau de Arellano J (2010) Formulation of the Dutch atmospheric large-eddy simulation (DALES) and overview of its applications. Geosci Model Dev 3:415–444

Holtslag A, Svensson G, Baas P, Basu S, Beare B, Beljaars A, Bosveld F, Cuxart J, Lindvall J, Steeneveld G, et al. (2013) Stable atmospheric boundary layers and diurnal cycles: challenges for weather and climate models. Bulletin of the American Meteorological Society 94(11):1691–1706

Holtslag AA (2003) Gabls initiates intercomparison for stable boundary layer case. GEWEX news 13(2):7–8

Holtslag B (2006) Preface: Gewex atmospheric boundary-layer study (gabls) on stable boundary layers. Boundary-Layer Meteorology 118(2):243–246

Huang J, Bou-Zeid E (2013) Turbulence and vertical fluxes in the stable atmospheric boundary layer. part i: a large-eddy simulation study. Journal of the Atmospheric Sciences 70(6):1513–1527

Jiménez M, Cuxart J (2005) Large-eddy simulations of the stable boundary layer using the standard kolmogorov theory: Range of applicability. Boundary-Layer Meteorology 115(2):241–261

Jiménez M, Cuxart J (2006) Study of the probability density functions from a large-eddy simulation for a stably stratified boundary layer. Boundary-layer meteorology 118(2):401–420

Kitamura Y (2010) Self-consistency validation of subgrid scale parameterization schemes in a large-eddy simulation. Journal of the Meteorological Society of Japan Ser II 88(5):813–825

Kolmogorov AN (1941) The local structure of turbulence in incompressible viscous fluid for very large reynolds numbers. Cr Acad Sci URSS 30:301–305

Kosović B, Curry JA (2000) A large eddy simulation study of a quasi-steady, stably stratified atmospheric boundary layer. Journal of the atmospheric sciences 57(8):1052–1068

Lacser A, Arya S (1986) A comparative assessment of mixing-length parameterizations in the stably stratified nocturnal boundary layer (nbl). Boundary-layer meteorology 36(1-2):53–70

Lazeroms WM, Svensson G, Bazile E, Brethouwer G, Wallin S, Johansson AV (2016) Study of transitions in the atmospheric boundary layer using explicit algebraic turbulence models. Boundary-Layer Meteorology 161(1):19–47

Lilly DK (1992) A proposed modification of the germano subgrid-scale closure method. Physics of Fluids A: Fluid Dynamics 4(3):633–635

Lilly K (1966) The representation of small-scale turbulence in numerical simulation experiments. NCAR

List RJ, et al. (1951) Smithsonian meteorological tables. Smithsonian miscellaneous collections

Lovejoy S, Tuck A, Hovde S, Schertzer D (2008) Do stable atmospheric layers exist? Geophysical Research Letters 35(1)

Lovejoy S, Tuck A, Schertzer D, Hovde S (2009) Reply to comment by igor esau on “do stable atmospheric layers exist?”. Geophysical research letters 36(11)

Lu H, Porté-Agel F (2011) Large-eddy simulation of a very large wind farm in a stable atmospheric boundary layer. Physics of Fluids 23(6):065,101

Lu H, Porté-Agel F (2014) On the development of a dynamic non-linear closure for large-eddy simulation of the atmospheric boundary layer. Boundary-layer meteorology 151(3):429–451

MacVean M (2003) Description of les arctic stable boundary layer case for gabls

Maronga B, Gryschka M, Heinze R, Hoffmann F, Kanani-Sühring F, Keck M, Ketelsen K, Letzel MO, Sühring M, Raasch S (2015) The parallelized large-eddy simulation model (PALM) version 4.0 for atmospheric and oceanic flows: model formulation, recent developments, and future perspectives. Geosci Model Dev 8:2515–2551

Maronga B, Knigge C, Raasch S (2020) An improved surface boundary condition for large-eddy simulations based on monin–obukhov similarity theory: Evaluation and consequences for grid convergence in neutral and stable conditions. Boundary-Layer Meteorology 174(2):297–325

Mason P, Derbyshire S (1990) Large-eddy simulation of the stably-stratified atmospheric boundary layer. Boundary-layer meteorology 53(1-2):117–162

Matheou G (2016) Numerical discretization and subgrid-scale model effects on large-eddy simulations of a stable boundary layer. Quarterly Journal of the Royal Meteorological Society 142(701):3050–3062

Matheou G, Chung D (2014) Large-eddy simulation of stratified turbulence. part ii: Application of the stretched-vortex model to the atmospheric boundary layer. Journal of the Atmospheric Sciences 71(12):4439–4460

Meneveau C, Lund TS, Cabot WH (1996) A lagrangian dynamic subgrid-scale model of turbulence. Journal of fluid mechanics 319:353–385

Miller NE, Stoll R (2013) Surface heterogeneity effects on regional-scale fluxes in the stable boundary layer: Aerodynamic roughness length transitions. Boundary-layer meteorology 149(2):277–301

Mironov DV, Sullivan PP (2016) Second-moment budgets and mixing intensity in the stably stratified atmospheric boundary layer over thermally heterogeneous surfaces. Journal of the Atmospheric Sciences 73(1):449–464

Muñoz-Esparza D, Kosović B, Mirocha J, van Beeck J (2014) Bridging the transition from mesoscale to microscale turbulence in numerical weather prediction models. Boundary-layer meteorology 153(3):409–440

Nieuwstadt FT (1984) The turbulent structure of the stable, nocturnal boundary layer. Journal of the atmospheric sciences 41(14):2202–2216

Park J, Basu S, Manuel L (2014) Large-eddy simulation of stable boundary layer turbulence and estimation of associated wind turbine loads. Wind Energy 17(3):359–384

Peña A, Gryning SE, Mann J, Hasager CB (2010) Length scales of the neutral wind profile over homogeneous terrain. Journal of Applied Meteorology and Climatology 49(4):792–806

Persson POG, Fairall CW, Andreas EL, Guest PS, Perovich DK (2002) Measurements near the atmospheric surface flux group tower at sheba: Near-surface conditions and surface energy budget. Journal of Geophysical Research: Oceans 107(C10):SHE–21

Pope SB (2001) Turbulent flows

Pope SB (2004) Ten questions concerning the large-eddy simulation of turbulent flows. New journal of Physics 6(1):35

Porté-Agel F, Meneveau C, Parlange MB (2000) A scale-dependent dynamic model for large-eddy simulation: application to a neutral atmospheric boundary layer. Journal of Fluid Mechanics 415:261–284

Porté-Agel F, Lu H, Wu YT (2010) A large-eddy simulation framework for wind energy applications. In: The fifth international symposium on computational wind engineering, vol 23

Porté-Agel F, Lu H, Wu YT (2013) Interaction between large wind farms and the atmospheric boundary layer. Mechanics 2210(9838)

Poulos GS, Blumen W, Fritts DC, Lundquist JK, Sun J, Burns SP, Nappo C, Banta R, Newsom R, Cuxart J, et al. (2002) Cases-99: A comprehensive investigation of the stable nocturnal boundary layer. Bulletin of the American Meteorological Society 83(4):555–582

Prandtl L (1925) Bericht über die entstehung der turbulenz. Z Angew Math Mech 5:136–139

Rodier Q, Masson V, Couvreux F, Paci A (2017) Evaluation of a buoyancy and shear based mixing length for a turbulence scheme. Frontiers in Earth Science 5:65

Rodrigo JS, Anderson PS (2013) Investigation of the stable atmospheric boundary layer at halley antarctica. Boundary-layer meteorology 148(3):517–539

Rodrigo JS, Churchfield M, Kosovic B (2017) A methodology for the design and testing of atmospheric boundary layer models for wind energy applications. Wind Energy Science 2(1):35

de Roode SR, Jonker HJJ, van de Wiel BJH, Vertregt V, Perrin V (2017) A diagnosis of excessive mixing in Smagorinsky subfilter-scale turbulent kinetic energy models. J Atmos Sci 74:1495–1511

Sagaut P (2006) Large eddy simulation for incompressible flows: an introduction. Springer Science & Business Media

Schalkwijk J, Jonker HJ, Siebesma AP, Van Meijgaard E (2015) Weather forecasting using gpu-based large-eddy simulations. Bulletin of the American Meteorological Society 96(5):715–723

Schumann U (1991) Subgrid length-scales for large-eddy simulation of stratified turbulence. Theoretical and Computational Fluid Dynamics 2(5-6):279–290

Smagorinsky J (1963) General circulation experiments with the primitive equations: I. the basic experiment. Mon Wea Rev 91:99–164

Sorbjan Z (2012) A study of the stable boundary layer based on a single-column k-theory model. Boundary-layer meteorology 142(1):33–53

Sorbjan Z (2014) Modelling of the evolving stable boundary layer. Boundary-layer meteorology 151(3):407–428

Steeneveld G, Van de Wiel B, Holtslag A (2006) Modelling the arctic stable boundary layer and its coupling to the surface. Boundary-layer meteorology 118(2):357–378

Steeneveld G, Van de Wiel B, Holtslag A (2007) Diagnostic equations for the stable boundary layer height: Evaluation and dimensional analysis. Journal of applied meteorology and climatology 46(2):212–225

Steinfeld G, Raasch S, Markkanen T (2008) Footprints in homogeneously and heterogeneously driven boundary layers derived from a lagrangian stochastic particle model embedded into large-eddy simulation. Boundary-layer meteorology 129(2):225–248

Sterk H, Steeneveld G, Holtslag A (2013) The role of snow-surface coupling, radiation, and turbulent mixing in modeling a stable boundary layer over arctic sea ice. Journal of Geophysical Research: Atmospheres 118(3):1199–1217

Stoll R, Porté-Agel F (2009) Surface heterogeneity effects on regional-scale fluxes in stable boundary layers: surface temperature transitions. Journal of the atmospheric sciences 66(2):412–431

Sullivan PP, Weil JC, Patton EG, Jonker HJ, Mironov DV (2016) Turbulent winds and temperature fronts in large-eddy simulations of the stable atmospheric boundary layer. Journal of the Atmospheric Sciences 73(4):1815–1840

Svensson G, Holtslag AA (2009) Analysis of model results for the turning of the wind and related momentum fluxes in the stable boundary layer. Boundary-layer meteorology 132(2):261–277

Udina M, Sun J, Kosović B, Soler MR (2016) Exploring vertical turbulence structure in neutrally and stably stratified flows using the weather research and forecasting–large-eddy simulation (wrf–les) model. Boundary-layer meteorology 161(2):355–374

Van Atta C, Chen W (1970) Structure functions of turbulence in the atmospheric boundary layer over the ocean. Journal of Fluid Mechanics 44(1):145–159

Von Kármán T (1930) Mechanische änlichkeit und turbulenz. Nachrichten von der Gesellschaft der Wissenschaften zu Göttingen, Mathematisch-Physikalische Klasse 1930:58–76

Wicker LJ, Skamarock WC (2002) Time-splitting methods for elastic models using forward time schemes. Mon Wea Rev 130:2088–2097

Van de Wiel B, Moene A, De Ronde W, Jonker H (2008) Local similarity in the stable boundary layer and mixing-length approaches: consistency of concepts. Boundary-layer meteorology 128(1):103–116

Wilson JM, Venayagamoorthy SK (2015) A shear-based parameterization of turbulent mixing in the stable atmospheric boundary layer. Journal of the Atmospheric Sciences 72(5):1713–1726

Xie S, Archer CL (2017) A numerical study of wind-turbine wakes for three atmospheric stability conditions. Boundary-Layer Meteorology 165(1):87–112